

September
2018
Volume 1 Issue 1





#### **Editor-in-Chief**

#### Shankar Chakraborty Jadavpur university, India

#### **Editorial Board Members**

Bounit Ahmed, Moroccan Fengxian Xin, China Liancun Zheng, China Farshad Abbasi, Iran Venanzio Giannella, Italy Milad Armin, UK Mohamed Kamal Ahmed, Egypt Hongping Hu, China Sathyashankara Sharma, India Paweł Grzegorz Kossakowski, Poland Jiusheng Bao, China Mohamed El-Amine Slimani, Algeria Rong Chen, China Ambreen Afsar Khan, Pakistan Pradeep Kumar Gautam, India Afshin Zeinedini, Iran Jinglun Fu, China Wuyi Wan, China Salah Aguib, Algeria MD Shamshuddin, India Wei Cao, China Ladeesh V G V G, India

Hao Wang, China
Kishore Debnath, India
Marcos Rodriguez Millan, Spain
Nima Ahmadi, Iran
Bing Yang, China
Bikash Sahoo, India
Muhammad-Asif, Pakistan
Asghar Farhadi, Iran
Krishna Lok Singh, India
Vipin Nair, India
Shahriar-Dastjerdi, Iran
Vinothkumar Sivalingam, India
Saad AbdelHameed EL-Sayed, Egypt

Baoshan Zhu, China

xinming zhang, China

Zhang Rongyun, China

XinJiang Lu, China Sedat Yayla, Turkey Lie Sun, China

Jan Awrejcewicz, Poland

Artur Portela, Brazil Seyed Masoud-Vahedi, Iran Kuo Liu, China

Mohamed Nabil Allam, Egypt

Arash Reza, Iran Reza Aghaei-Togh, Iran Jun Peng, China

Hossein Hemmatian, Iran Mousa Khalifa Ahmed, Egypt Mohammed Diany, Morocco

Yinghong Peng, China

Mohammed Zubairuddin, India

Catalin Iulian Pruncu, UK Ashok Malleshappa Hulagabali, India

Mohammad Nimafar, Iran Ahad Gholipoor, Iran Xuejun Jason Liu, USA Md Muslim Ansari, India Humaira Yasmin, Saudi Arabia

Hamdy Mahmoud Youssef, Egypt

Shuang Li, China Daniele Cafolla, Italian Yu-Chun Kung, USA

Fuji Wang, China

Abdelkader xx Doudou, Morocco Mohamed Ibrahim Othman, Egypt

Wenbin Wang, China

Elammaran Jayamani, Malaysia

Guang Yih Sheu, Taiwan Xikun Wang, China Amr Kaood, Egypt Chew Kuew Wai, Malaysia

Pramod Ramchandraji Pachghare, India Anna Valentinovna Morozova, Russia

Allila valelitillovila Morozova, Russia

Michael Raj F, India

Varinder Kumar Singh, India

Yuan Kang, China

Kutsİ Savaş Erduran, Turkey

Siavash Azimi, Iran

Philemon Kazimil Mzee, Tanzania Raj Rani Bhargava, India Majid Jabbari, Iran Mohaned El wazziki, Canada

Gurmeet Singh, India Uziel Yuri Sandler, Israel Satish Kumar, India Ikram Ullah, Pakistan Shubhashis Sanyal, India Xinhong Yang, China

Lyudmila Ivanovna Gracheva, Ukraine Milon Selvam Dennison, India

Yan Zhao, China

Alfaisal Abdelhameed Mohamed

Hasan, UAE

Khalil Ur Rehman, Pakistan Pravin Tukaram Nitnaware, India João Roberto Sartori Moreno, Brasil

Ravinder Kumar, India Samad Nadimi Bavil Oliaei, Turkey

Zichen Deng, China

Sasan Yousefi Barfroushi, Iran Asit Kumar Parida, India Samuel Filgueiras Rodrigues, Canada

Ravindra Jilte, India

Gadang Priyotomo, Indonesia Asim Mukhopadhyay, India

Nan Wu, Canada Yihua Cao, China Tso-Liang Teng, Taiwan Vahid Tahmasbi, Iran Matteo Strozzi, Italy Santosh N.Shelke, India Huang Youliang, China Enock Andrews Duodu, Ghana

Akba Salemi, Iran Ramin Kouhikamali, Iran Mehdi Safari, Iran Alper Uysal, Turkey Baskaran Ayyalusamy, India

Arnaldo Casalotti, Italy

# Journal of Mechanical Engineering Research

**Editor-in-Chief** 

Shankar Chakraborty





#### Volume 1 | Issue 1 | September 2018 | Page 1-32

#### Journal of Mechanical Engineering Research

#### **Contents**

#### Article

- 1 A New Viscoelastic Model for Polycarbonate Compressing Flow Wei Cao Yaqiang Shen Shixun Zhang Tao Wang Yakun Wu Changyu Shen
- 9 Finite Element Analysis of Stuffing-box Packing Subjected to Thermo-mechanical Loads

  Kaputar Pahoum Mohammad Diany Mustanha Mahrauki

Kaoutar Bahoum Mohammed Diany Mustapha Mabrouki Jaouad Azouz

16 Some Aspects of Fretting Fatigue under complex cyclic contact load condition

Farshad Abbasi

#### **Review**

22 Remark On Optimal Homotopy Method: Application Towards
Nano-Fluid Flow Narrating Differential Equations
Farah Jabeen Awan Asif Mehmood and Khalil Ur Rehman

**28** The Influence of the Two-child Policy on Urbanization in China Kaiyong Wang Hu Yu

#### Copyright

**Journal of Mechanical Engineering Research** is licensed under a Creative Commons-Non-Commercial 4.0 International Copyright (CC BY- NC4.0). Readers shall have the right to copy and distribute articles in this journal in any form in any medium, and may also modify, convert or create on the basis of articles. In sharing and using articles in this journal, the user must indicate the author and source, and mark the changes made in articles. Copyright © BILINGUAL PUBLISHING CO. All Rights Reserved.



#### Journal of Mechanical Engineering Research

http://ojs.bilpublishing.com/index.php/jmer



1

#### **ARTICLE**

#### A New Viscoelastic Model for Polycarbonate Compressing Flow

#### Wei Cao<sup>1</sup>\* Yaqiang Shen<sup>2</sup> Shixun Zhang<sup>1</sup> Tao Wang<sup>3</sup> Yakun Wu<sup>1</sup> Changyu Shen<sup>1</sup>

- 1. National Engineering Research Center of Mold & Die, Zhengzhou University, Zhengzhou, Henan, 450002, China
- 2. Shenzhen Zhaowei Machinery & Electronics CO., LTD., Shenzhen, 518103, China
- 3. Beijing Institute of Aeronautical Materials, Beijing, 100095, China

#### ARTICLE INFO

#### Article history:

Received: 1 November 2018 Accepted: 9 November 2018 Published: 30 November 2018

#### Keywords: Viscoelastic Constitutive model Compressing flow Numerical simulation

#### ABSTRACT

To overcome the weakness of conventional models in describing compressing flow especially in start and end stages the shear rate derivative was added to the right side of the PTT constitutive equation. The ability of describing the well-known 'shear thinning' and 'stretch harden' phenomena was first illustrated by theoretical analysis. Then the governing equations for compressing flow were established in terms of incompressible and isothermal fluid, and the numerical method was constructed to discretize the equations and get the compressing flow solutions. In order to validate the model and numerical methods the experiments with four melt temperatures were conducted and the corresponding simulations were performed. The better agreements with experimental data indicates the modified PPT model is better than the original PTT model in prediction of compressing flow. In addition, the proposed model is also validated with low and high compressing speed experiments.

#### 1. Introduction

ransparent polycarbonates (PC) have been widely used in optical engineering. In order to reduce the residual stresses which influence the optical properties, the injection/compression process is often applied in manufacturing transparent PC products. This process is divided into two successive stages: injection and compression. The rheological characteristics of polymer in injection period have been studied extensively by both experiments and simulations. The rheological behaviors in compression, however, have not received much attention

because the process has only been applied in recent years. Some softwares such as Moldflow usually applies the uniform rheological model, for example, Cross-WLF model<sup>[1]</sup> to describe the rheological behaviors in the two different stages for convenience. But polycarbonate in compression has special characteristic which are different from injection as our previous work<sup>[2]</sup> exhibited. It is necessary to characterize it with an appropriate model so as to control the manufacturing precisely. Therefore, a new viscoelastic model based on Phan-Thien–Tanner model<sup>[3-4]</sup> for PC compression was constructed in this study.

National Engineering Research Center of Mold & Die, Zhengzhou University,

Zhengzhou, Henan, China;

E-mail: wcao@zzu.edu.cn.

Fund Project:

Financial supports from the National Science Foundation of China (No. 11672271, 11432003) The National Key Research and Development Program of China (No. 2016YFB0101602) for this research work are gratefully acknowledged.

<sup>\*</sup>Corresponding Author:

Some researches have shown polymer melt exhibits viscoelasticity during compression<sup>[5-9]</sup>. There are lots of viscoelastic models to describe the rheological behavior, such as Giesekus, Leonov, Oldroyd-B, extended Pom-Pom (XPP) and Phan-Thien-Tanner (PTT), but none of them has proven to be superior to others in describing all kinds of flow[10]. Aboubacar et al. found the PTT model was better than the Oldroyd-B model in describing planar contraction flows with high Weissenberg number<sup>[11]</sup>. Palmer and Phillips demonstrated PTT model was suitable to describe the flow combined shear and elongation characteristics<sup>[12]</sup>. Furthermore, Cao and Kobayashi found that this model can well predict flow-induced stresses for non-equilibrium flow in injection molding<sup>[13-14]</sup>. Thus the PTT model was used to as the base model for revision in this study.

Recently we found the compressing force varies as 'steep—steady —steep—steady' pattern, and none of current constitutive can describe the two steep increasing regions well<sup>[2]</sup>. In addition we also found there was no significant difference between the popular viscoelastic models such as Leonov, PTT, XPP for compressing flow. It was found the shear rate changed rapidly in the two force unusual increasing regions through careful calculations. This drove us to account for the additional shear rate contribution by adding its derivative to the right side of the PTT constitutive equation just like the Oldroyd-B model did[15]. The modified model combines both nonlinear viscoeastic characteristics of PTT and the capability of characterizing the rapid shear rate. Usually the reasonability of the proposed model requires to be demonstrated by theoretical analysis and experimental test. The nonlinear characteristic makes the analysis very difficult, but linearization and dimensionless methods can solve this problem efficiently especially for viscoelastic flow problem<sup>[16-19]</sup>. The proposed model was first analyzed to be able to describe the well-known 'shear thinning' and 'stretch harden' phenomena. Then the numerical simulations and experiments were carried out to illustrate the validation. The comparisons were conducted with different melt temperatures and compressing speeds.

#### 2. Modified PTT Model

In our previous work we found the compressing force exhibits abnormal increase in compression start and end stage due to irregular changes of shear rate, and neither viscous nor viscoelastic existing models can describe this phenomenon properly. Meanwhile it also showed the compressing flow exhibited nonlinear viscoelastic characteristics. Thus we revised the PTT model by adding the shear rate derivative term  $\lambda^{\frac{1}{3}}$  at the right side of the

constitutive equation to account for the effects of rapid changes of shear rate  $\dot{\gamma}$ .

$$\left[1 + \frac{\lambda \epsilon}{\eta} tr(\tau)\right] \tau + \lambda \overset{\nabla}{\tau} = 2\eta \left(\dot{\gamma} + \lambda \dot{\dot{\gamma}}\right)$$
 (1)

here  $\epsilon$  is the nonlinear parameter to eliminate the singularity in extensional viscosity,  $tr(\tau)$  denotes the trace of the viscoelastic tensor  $\tau$ ,  $\lambda$ ,  $\eta$  represent the relaxation time and viscosity coefficient respectively, and  $\lambda'$  is the parameter to control the effect of shear rate derivative. The upper convective derivative is defined as

$$\overset{\nabla}{\mathbf{\tau}} = \frac{\partial \mathbf{\tau}}{\partial t} + \mathbf{v} \cdot \nabla \mathbf{\tau} - \nabla \mathbf{v} \cdot \mathbf{\tau} - \mathbf{\tau} \cdot (\nabla \mathbf{v})^{T}$$
(2)

In order to verify the reasonability of the proposed model, we first illustrate whether it is capable to characterize the well-known phenomena of 'shear thinning' and 'stretch harden'.

#### 2.1 Shear Thinning

For steady shear flow  $u = \dot{\gamma}y, v = 0$  the constitutive equations are reduced to

$$\left(1 + \frac{\lambda \epsilon}{\eta} \left(\tau_{xx} + \tau_{yy}\right)\right) \tau_{xx} - 2\lambda \dot{\gamma} \tau_{xy} = -2\eta \lambda \dot{\gamma}^2$$
(3)

$$\left(1 + \frac{\lambda \epsilon}{\eta} \left(\tau_{xx} + \tau_{yy}\right)\right) \tau_{xy} - \lambda \dot{\gamma} \tau_{yy} = \eta \dot{\gamma}$$
(4)

$$\left(1 + \frac{\lambda \epsilon}{\eta} \left(\tau_{xx} + \tau_{yy}\right)\right) \tau_{yy} = 0$$
(5)

The nominal solution for this problem is

$$\left(1 + \frac{\lambda \epsilon}{\eta} \tau_{xx}\right)^2 \tau_{xx} + 2\left(1 + \frac{\lambda \epsilon}{\eta} \tau_{xx}\right) \lambda' \eta \dot{\gamma}^2 - 2\lambda \eta \dot{\gamma}^2 = 0 \tag{6}$$

$$\tau_{xy} = \frac{\eta \dot{\gamma}}{1 + \frac{\lambda \epsilon}{n} \tau_{xx}} \tag{7}$$

$$\tau_{yy} = 0 \tag{8}$$

The Eq. (6) is a cubic equation about the stress component of  $\tau_{xx}$  and can be solved with algebraic method, the solution is

$$\tau_{xx} = \frac{\eta}{\lambda \epsilon} \left[ 1 + \left( 27\lambda - 9\lambda^{2} \right) \lambda \epsilon \dot{\gamma}^{2} + 3\lambda \epsilon^{\frac{1}{2}} \dot{\gamma} \sqrt{6 + \left( -8 + 9\left( \frac{3\lambda}{\lambda^{2}} - 1 \right)^{2} \right) \lambda^{2} \epsilon \dot{\gamma}^{2} + 24\lambda \lambda^{2} \epsilon^{3} \dot{\gamma}^{4}} \right]^{\frac{1}{3}}$$

$$(9)$$

Then the stress component  $\tau_{xy}$  can be determined

$$\tau_{xy} = \frac{\eta \dot{\gamma}}{1 + \left[1 + \left(27\lambda - 9\lambda^{2}\right)\lambda\epsilon \dot{\gamma}^{2} + 3\lambda\epsilon^{\frac{1}{2}}\dot{\gamma}\sqrt{6 + \left(-8 + 9\left(\frac{3\lambda}{\lambda^{2}} - 1\right)^{2}\right)\lambda^{2}\epsilon \dot{\gamma}^{2} + 24\lambda\lambda^{3}\epsilon^{3}\dot{\gamma}^{4}}\right]^{\frac{1}{3}}}$$

On using Eq. (10) the shear viscosity  $\eta_{sh} \left(=\tau_{xy}/\dot{\gamma}\right)$  is

calculated by

$$\eta_{sh} = \frac{\eta}{1 + \left[1 + \left(27\lambda - 9\lambda^{2}\right)\lambda\epsilon\dot{\gamma}^{2} + 3\lambda\epsilon^{\frac{1}{2}}\dot{\gamma}\sqrt{6 + \left(-8 + 9\left(\frac{3\lambda}{\lambda^{2}} - 1\right)^{2}\right)\lambda^{2}\epsilon\dot{\gamma}^{2} + 24\lambda\lambda^{3}\epsilon^{3}\dot{\gamma}^{4}}\right]^{\frac{1}{3}}}$$

This formula means the viscosity decreases with increasing shear rate  $\dot{\gamma}$ , which indicates the model can describe 'shear thinning' effect.

#### 2.2 Stretch Harden

For steady extension flow  $u=\dot{\varepsilon}x, v=-\frac{1}{2}\dot{\varepsilon}y, w=-\frac{1}{2}\dot{\varepsilon}z$ , the modified PTT model is reduced to

$$\left(1 + \frac{\lambda \epsilon}{n} \left(\tau_{xx} + \tau_{yy} + \tau_{zz}\right)\right) \tau_{xx} - 2\lambda \dot{\epsilon} \tau_{xx} = 2\eta \dot{\epsilon} \left(1 - 2\lambda' \dot{\epsilon}\right)$$
 (12)

$$\left(1 + \frac{\lambda \epsilon}{\eta} \left(\tau_{xx} + \tau_{yy} + \tau_{zz}\right)\right) \tau_{xy} - \frac{1}{2} \lambda \dot{\epsilon} \tau_{xy} = 0$$
(13)

$$\left(1 + \frac{\lambda \epsilon}{n} \left(\tau_{xx} + \tau_{yy} + \tau_{zz}\right)\right) \tau_{xz} - \frac{1}{2} \lambda \dot{\epsilon} \tau_{xz} = 0$$
 (14)

$$\left(1 + \frac{\lambda \epsilon}{\eta} \left(\tau_{xx} + \tau_{yy} + \tau_{zz}\right)\right) \tau_{yy} + \lambda \dot{\varepsilon} \tau_{yy} = -\eta \dot{\varepsilon} \left(1 + \lambda' \dot{\varepsilon}\right)$$
 (15)

$$\left(1 + \frac{\lambda \epsilon}{\eta} \left(\tau_{xx} + \tau_{yy} + \tau_{zz}\right)\right) \tau_{yz} + \lambda \dot{\varepsilon} \tau_{yz} = 0$$
 (16)

$$\left(1 + \frac{\lambda \epsilon}{n} \left(\tau_{xx} + \tau_{yy} + \tau_{zz}\right)\right) \tau_{zz} + \lambda \dot{\varepsilon} \tau_{zz} = -\eta \dot{\varepsilon} \left(1 + \lambda' \dot{\varepsilon}\right)$$
 (17)

Eqs. (13) - (14) indicate . Substituting this formula to Eq. (12) and Eqs. (15) – (16) yields

$$\tau_{xx} = -\frac{4\eta \left(1 - 2\lambda' \dot{\varepsilon}\right)}{3\lambda} \tag{18}$$

$$\tau_{yy} = -\frac{2\eta \left(1 + \lambda' \dot{\varepsilon}\right)}{3\lambda} \tag{19}$$

$$\tau_{zz} = -\frac{2\eta \left(1 + \lambda' \dot{\varepsilon}\right)}{3\lambda} \tag{20}$$

$$\tau_{vz} = 0 \tag{21}$$

The extension viscosity can be determined

$$\eta_{\rm ex} = \frac{\tau_{\rm xx}}{\dot{\varepsilon}} = \frac{4\eta}{3\lambda} \left( 2\lambda' - \frac{1}{\dot{\varepsilon}} \right) \tag{22}$$

This formula indicates the extension viscosity increases as the extension rate  $\dot{\varepsilon}$  increases, which means the model can describe 'stretch harden' behavior.

#### 3. Compressing Flow Simulation

In this study, the fully filled PC fluid was compressed at a constant velocity  $(\dot{h})$  and flow out at disc brims, shown as Fig. 1. The melt flow was limited within the geometric region:  $0 \le r \le R$  and  $\le z \le h(t)$ . The compressing flow was, due to the changing height h(t), inherently transient and inhomogeneous flows.

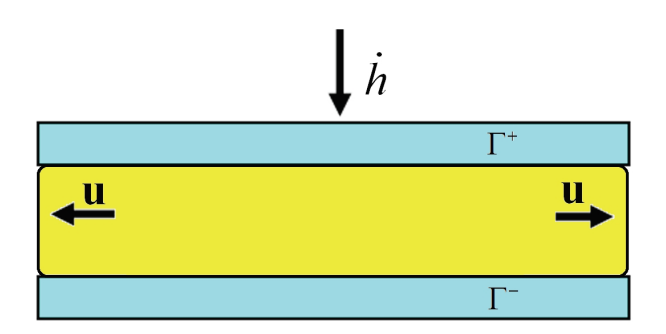


Figure 1. Schematic illustration of fully compressing flow.

#### 3.1 Governing Equations

Compared with viscous force the gravitational and inertial forces are small and ignored. The governing equations for isothermal, incompressible and viscoelastic flow in cylindrical coordinates can be written

$$\frac{1}{r}\frac{\partial}{\partial r}(rv_r) + \frac{\partial}{\partial z}v_z = 0 \tag{23}$$

$$-\frac{\partial p}{\partial r} + \frac{1}{r} \frac{\partial}{\partial r} (r \tau_{rr}) + \frac{\partial}{\partial z} \tau_{zr} = 0$$
 (24)

$$-\frac{\partial p}{\partial z} + \frac{1}{r} \frac{\partial}{\partial r} (r \tau_{rz}) + \frac{\partial}{\partial z} \tau_{zz} = 0$$
 (25)

here r and z are the radial and axial coordinates respectively,  $v_r$  and  $v_z$  are the corresponding velocity components, p is the pressure, and  $\tau_{rr}$ ,  $\tau_{rz}$  and  $\tau_{zz}$  are the stress components.

During compression the container keeps open at the edges, therefore the pressure at the disc rim can be assumed zero.

$$p = 0 \text{ at } r = R \tag{26}$$

No slip boundary conditions for radial velocity were used on both top and bottom discs.

$$v_r = 0, v_z = 0 \text{ at } z = 0 \left(\Gamma^{-1}\right) \tag{27}$$

$$v_r = 0, v_z = \dot{h} \text{ at } z = h \left( \Gamma^+ \right)$$
 (28)

In this study, the compressing velocity of the upper disc keeps constant, i.e.  $v_z = \dot{h} = \frac{dH}{dt} \equiv const$ . Thus all the axial ve-

locity  $v_z$  at the same level is equal, which means  $\frac{\partial v_z}{\partial r} = 0$ .

#### 3.2 Stresses

The stress tensor in viscoelastic fluid can be expressed as a sum of Newtonian and viscoelastic components:

$$\sigma = \tau_s + \tau_v \tag{29}$$

here  $\tau_v$  is the extra stress tensor due to viscoelasticity and  $\tau_s$  is the stress component of a Newtonian fluid given by

$$\mathbf{\tau}_{s} = 2\eta_{s}\dot{\mathbf{\gamma}} \tag{30}$$

The viscoelastic stress tensor is the sum of different modes

$$\mathbf{\tau}_{v} = \sum_{i} \mathbf{\tau}_{i} \tag{31}$$

The ith mode stress  $\tau_i$  is governed by modified PTT

model

$$\left[1 + \frac{\lambda_i \epsilon}{\eta_i} tr(\tau_i)\right] \tau_i + \lambda_i \overset{\nabla}{\tau_i} = 2\eta_i \left(\dot{\gamma} + \lambda \overset{\nabla}{\dot{\gamma}}\right)$$
(32)

here  $\lambda_i$ ,  $\eta_i$  are the relaxation time and viscosity coefficient of ith mode.

#### 3.3 Numerical Method

The momentum equations (24)–(25) subject to stress expression can be written as

$$-\frac{\partial p}{\partial r} + 2\eta_s \frac{\partial^2 v_r}{\partial r^2} + \eta_s \frac{\partial^2 v_r}{\partial z^2} + \sum_{i=1}^M \left( \frac{\partial \tau_{i,rr}}{\partial r} + \frac{\partial \tau_{i,rz}}{\partial z} \right) = 0$$
 (33)

$$-\frac{\partial p}{\partial z} + \eta_s \frac{\partial^2 v_r}{\partial r \partial z} + 2\eta_s \frac{\partial^2 v_z}{\partial z^2} + \sum_{i=1}^M \left( \frac{\partial \tau_{i,rz}}{\partial r} + \frac{\partial \tau_{i,zz}}{\partial z} \right) = 0 \quad (34)$$

Due to the coupled relationship between velocity, pressure and stress in governing equations and constitutive equations and the nonlinearity the analytical solutions for compressing flow can hardly be obtained even for a simple flow. The numerical methods have to be used to determine the discrete solutions. In this study, the finite difference method (FDM) was employed to determine the numerical solution because the PC flow was limited within a cylindrical rectangular region  $0 \le r \le R$ ;  $h \le z \le H$ , which is suitable for FDM calculation. To keep the numerical consistence and stability, the forward difference and central difference schemes were used to discretize the one order and two order differential terms respectively, and the 'up-wind' scheme was used to discretize the convective term in constitutive equations. The differential equations corresponding to mass conservative equation (23), momentum equations (33)-(34) and constitutive equation (32) were discretized as

$$\frac{1}{r_{I}} \frac{v_{r,ij}^{n} - v_{r,i-1j}^{n}}{\Delta r} + v_{r,i}^{n} + \frac{v_{z,ij}^{n} - v_{z,ij-1}^{n}}{\Delta z} = 0$$
 (35)

$$-\frac{p_{ij}^{n}-p_{i-1j}^{n}}{\Delta r}+2\eta_{s}\frac{v_{r,i-1j}^{n}-2v_{r,ij}^{n}+v_{r,i+1j}^{n}}{\Delta r^{2}}+\eta_{s}\frac{v_{r,ij-1}^{n}-2v_{r,ij}^{n}+v_{r,ij+1}^{n}}{\Delta z^{2}}+\eta_{s}\frac{v_{r,ij-1}^{n}-2v_{r,ij}^{n}+v_{r,ij+1}^{n}}{\Delta z^{2}}+\eta_{s}\frac{v_{r,ij-1}^{n}-2v_{r,ij+1}^{n}}{\Delta z^{2}}+\eta_{s}\frac{v_{r,ij-1}^{n}}{\Delta z^{2}}+\eta_{s}\frac{$$

$$\sum_{k} \left( \frac{\tau_{k,rr,ij}^{n} - \tau_{k,rr,i-1j}^{n}}{\Delta r} + \frac{\tau_{k,rr,ij}^{n} - \tau_{k,rz,ij-1}^{n}}{\Delta z} \right) = 0$$
 (36)

$$-\frac{p_{ij}^{n}-p_{ij-1}^{n}}{\Delta z}+\eta_{s}\frac{v_{r,i+1\,j+1}^{n}+v_{r,i-1\,j-1}^{n}-v_{r,i-1\,j+1}^{n}-v_{r,i+1\,j-1}^{n}}{\Delta r\Delta z}+$$

$$2\eta_{s} \frac{v_{zij-1}^{n} - 2v_{zij}^{n} + v_{zij+1}^{n}}{\Delta z^{2}} + \sum_{k} \left( \frac{\tau_{k,rz,ij}^{n} - \tau_{k,rz,i-1,j}^{n}}{\Delta r} + \frac{\tau_{k,zz,ij}^{n} - \tau_{k,zz,ij-1}^{n}}{\Delta z} \right) = 0$$

(37)

(32) 
$$\left[1 + \frac{\lambda_k \epsilon}{\eta_k} tr(\boldsymbol{\tau}_k^n)\right] \boldsymbol{\tau}_k^n + \lambda_k \frac{\boldsymbol{\tau}_k^n - \boldsymbol{\tau}_k^{n-1}}{\Delta t} + \boldsymbol{v}_{ij}^{n-1} \cdot \left(\frac{\left(\boldsymbol{\tau}_{k,ij}^n - \boldsymbol{\tau}_{k,i-1j}^n\right)/\Delta r}{\left(\boldsymbol{\tau}_{k,ij}^n - \boldsymbol{\tau}_{k,ij-1}^n\right)/\Delta z}\right) -$$

$$\left(\frac{\left(\mathbf{v}_{ij}^{n}-\mathbf{v}_{i-1j}^{n}\right)}{\Delta r} \quad \frac{\left(\mathbf{v}_{ij}^{n}-\mathbf{v}_{i-1j}^{n}\right)}{\Delta z}\right) \cdot \boldsymbol{\tau}_{k}^{n}-\boldsymbol{\tau}_{k}^{n} \cdot \left(\frac{\left(\mathbf{v}_{ij}^{n}-\mathbf{v}_{i-1j}^{n}\right)}{\Delta r}\right) = 2\eta_{k}\left(\dot{\gamma}+\lambda\dot{\dot{\gamma}}\right)$$

$$\frac{\left(\mathbf{v}_{ij}^{n}-\mathbf{v}_{i-1j}^{n}\right)}{\Delta z}\right) = 2\eta_{k}\left(\dot{\gamma}+\lambda\dot{\dot{\gamma}}\right)$$
(38)

As the stress trace  $tr(\tau_k^n)$  was also unknown, the above algebraic equations are nonlinear and the Newton-Raphson iterative method was employed to determine the solutions.

When all the solutions for discrete nodes were determined, the vertical force at every node of upper disc was calculated with the following formula

$$F_{jk} = \left[ p_{jk} + \sum_{i=1}^{M} (\tau_{i,rz} + \tau_{i,zz})_{jk} \right]$$
 (39)

Then integrate the discrete force  $F_{jk}$  with bilinear interpolation scheme to get the compressing force imposed on the upper disc.

$$F_{comp} = \iint_{A_{+}} F_{jk}(r,z) dA \tag{40}$$

#### 4. Results and Discussion

#### 4.1 Experiments Set Up

ARES G2 rheometer (TA Instruments) was used to examine the melt rheological behavior during compressing. It cannot measure the viscosity or modulus in the process directly, but the compression force which closely relates the melt stress can be measured if the configuration is properly set up. On the other hand, this force can be calculated with formula (40) through discretization of the constitutive model and governing equations. Compare

270°C		280°C		290°C		300°C		310°C	
Relaxation $time \lambda_i(s)$	Modulus G <sub>i</sub> (Pa)	Relaxation time $\lambda_i$ (s)	Modulus G <sub>i</sub> (Pa)	Relaxation time $\lambda_i$ (s)	Modulus G <sub>i</sub> (Pa)	Relaxation time $\lambda_i$ (s)	Modulus G <sub>i</sub> (Pa)	Relaxation time $\lambda_i$ (s)	Modulus G <sub>i</sub> (Pa)
5.02923	76.5606	4.73195	51.3094	4.15657	46.913	3.0891	40.0322	2.0203	35.5218
0.583092	70.8121	0.22218	108.292	0.41924	50.135	0.363904	42.1809	0.31873	35.7013
5.56E-03	81150	9.52E-3	17602.6	5.59E-03	20158.2	8.97E-3	2983.95	3.57E-3	1867.95
8.56E-04	494619	9.05E-4	398497	6.77E-04	381588	5.83E-4	218261	4.63E-4	174874

**Table 1.** Measured relaxation times and moduli of 5 melt tem peratures with ARES G2.

**Table 2.** Simulated precisions of the two models for the four temperatures at compressing speed 0.01 mm/s

		P	ГΤ		Modified PTT			
Temperature $(^{\circ}\mathbb{C})$		Difference		Variance	Difference			Variance
,	Average	Start	End		Average	Start	End	variance
270	0.144836	0.464944	0.21165	0.014601	0.030326	0.025992	0.135206	0.003148
280	0.110653	0.144768	0.14169	0.004173	0.030326	0.075748	0.044342	0.000564
290	0.040754	0.13687	0.04062	0.00122	0.020929	0.035929	0.021636	0.000213
300	0.043427	0.022662	0.11008	0.001444	0.02439	0.013815	0.019223	0.000222

the differences between measured and simulated data can evaluate the correctness and advantages of the constitutive model.

The specimen was a thin disc with a diameter of 25 mm, and the compression started from 1.43 mm and stopped at 1.0 mm. To avoid polymer melt absorbing moisture in the air, the nitrogen was sweeping the disc during experiments. The rectangle of  $r \times h$  in a cylindrical coordinate system was discretized to  $100 \times 20$  small rectangles for FDM simulation.

The experimental material was polycarbonate, OQ 2720, Saibic Inc. The rotating rheological experiments were first carried out at melt temperatures of 270 °C, 280 °C, 290 °C and 300 °C to get the corresponding relaxation times and moduli listed in Tab. 1. Then the compressing experiments were performed at the four temperatures with compressing speed 0.01 mm/s. These experimental data were used to fit modified model and get the most appropriate constants  $\lambda' = 0.561$  and  $\epsilon = 0.425$ . To validate the proposed model, the additional experiments were conducted with compressing velocities of 0.005mm/s and 0.02mm/s at 300 °C.

#### **4.2 Melt Temperature Effects**

Fig. 2 shows the compressing forces vary in the same trend for different melt temperatures, i.e. rapid increase at the onset, steady growth in the middle stage and rapid increase again at the end. Both PTT and modified PTT models can correctly predict this tendency but the simulated precisions have significant differences, see Tab. 2. The average simulated precisions have been improved 2~3 times

by modifying PTT. The remarkable differences happen in the compression start and end stages which shear rate varies violently, for example, the simulated difference of modified PTT for 270 °C is 0.025992 at start compressing stage, this value of the original PTT rises to 0.464944, almost twenty times of the modified model. In addition, the average simulated variances for PTT model ars 4~8 times of the modified model for the four melt temperatures. Both Fig.2 and Tab. 2 indicate the modified PTT model better describes the rheological behavior than the original PPT model.

At the beginning of compression, the compressing force does not transfer to the bottom plate instantly and only the melt near the upper disc begins to flow, so the shear rates of the moving layers changes rapidly during this period. When all the melt within in the two discs flows to the brim the shear rate changes little, which do not cause much stress variation, and the compressing force increase steadily in the middle stage. Due to the gap is remarkable reduced in the end stage, the shear rate changes sharply again. For example, the decrease rate and increase rate of shear rate for 290 °C melt temperature reach 0.01658 and 0.00137 at the start and end stages respectively, which are considerable larger than the increase rate of 0.00041 in the middle stage, see Fig. 3. The violent changes of shear rate can influence the shear stresses and the close related compressing forces subsequently. Due to the contribution of shear rate change  $\dot{\vec{r}}$  was accounted, the modified PTT model significantly improved the simulating precisions especially at the start and end stages.

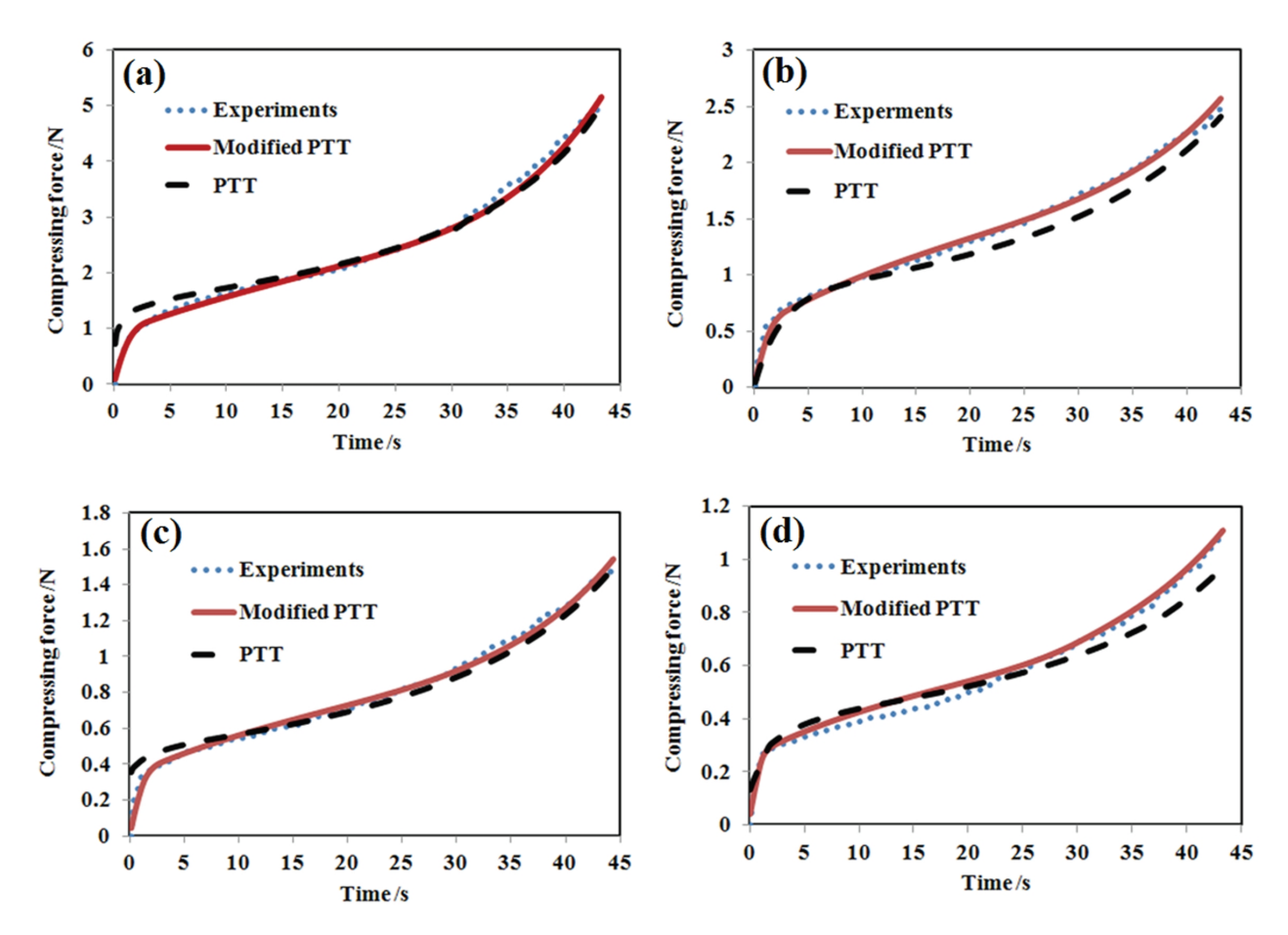


**Figure 2.** Compressing force varies with time for PC at compressing speed 0.01 mm/s with melt temperatures: (a) 270 °C; (b) 280 °C; (c) 290 °C; (d) 300 °C.

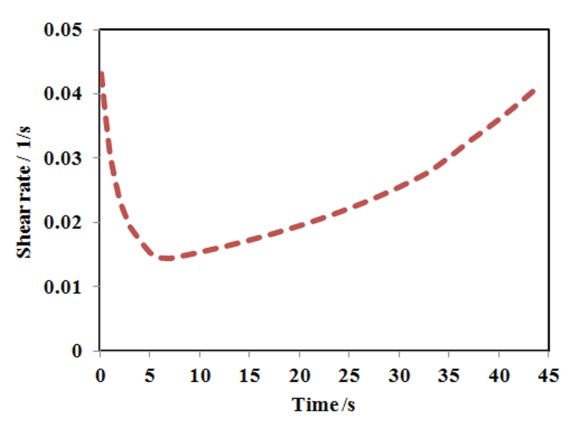


**Figure 3.** Simulated shear rate evolution near the center of upper disc at compressing speed 0.01 mm/s and melt temperature 290 °C

#### 4.3 Compressing Speed Effects

To validate the modified PTT model determined by 0.01 mm/s compressing speed the other two experiments with compressing speeds of 0.005 and 0.02 mm/s were carried out at melt temperatures of 300 °C. The measured com-

pressing forces for these two speeds exhibited unstable growth especially at start stage for low speed and middle stage for high speed which can be hardly simulated by any constitutive model, see Fig. 4. So the simulated compressing force profiles are less precise than that of the same temperature with compressing speed 0.01 mm/s shown as Fig. 2 (d).

The simulated precisions of the two models for the three speeds were listed in Tab. 3. Once again Tab. 3 shows the modified PTT model is superior to the original model for any compressing speed as shear rate derivative  $\frac{1}{2}$  was accounted in this model. Both average simulated differences and variances increase with increasing compression speeds either with PTT model or modified PTT model. When the compressing speed increases from 0.005 mm/s to 0.01 mm/s the average differences to experimental data for both models increase very little, but the variances rise about 3 and 2 times respectively. When the compressing speed continually increases to 0.02 mm/s the average simulated differences increase about 2 times of 0.005 mm/s, and the variances rise to about 21 and 10

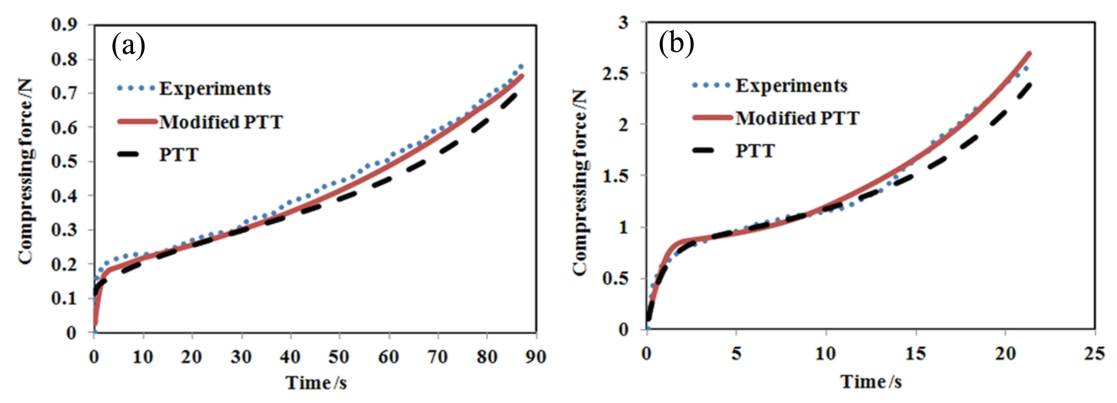


**Figure 4.** Compressing force varies with time for PC at melt temperature 300 °C with compressing speeds (a) 0.005 mm/s; (b) 0.02 mm/s

**Table 3.** Simulated precisions of the two models for the compressing speeds at temperature 300 °C

Compressing speed (mm/s)		P	ГТ		Modified PTT			
	Difference			Variance	Difference			Variance
	Average	Start	End	variance	Average	Start	End	variance
0.005	0.042634	0.045307	0.06339	0.000455	0.02059	0.027009	0.017221	0.000105
0.01	0.043427	0.022662	0.11008	0.001444	0.02439	0.013815	0.019223	0.000222
0.02	0.090167	0.079778	0.24856	0.009774	0.04460	0.063314	0.03559	0.001004

times of the low speed respectively. Because the measured data gets increasingly unstable as compressing speed increases, the simulated difference grows with the speed. Thus increasing the compressing speed can not get the credible data.

#### 5. Conclusion

As the poor ability of the conventional constitutive models in describing the rheological behaviors in compressing start and end stages, the new viscoelastic model was proposed to overcome the shortage in this study. The shear rate derivative was added in the right side of PTT constitutive model to calculate the additional stresses induced by shear rate changes. The experimental results showed the modification improved simulating precisions especially for the compressing start and end stages. This study indicates the shear rate changes should be considered in constructing constitutive equations for unsteady flow. In addition, the flow becomes more unsteady when the compressing speed increases, which also makes the simulated differences increase.

#### Reference

- A.I. Isayev and R.K. Upadhyay, Injection and Compression Molding Fundamentals, Marcel Deker, New York, 1987.
- [2] W. Cao, T. Wang, Y. Yan, et al. Evaluation of typical rhe-

- ological models fitting for polycarbonate squeeze flow. J. Applied Polymer Sci. 2015, 132(29): 42279(1-8).
- [3] N. Phan-Thien, and R.I. Tanner, An analytical solution for fully developed from network theory, J. Non-Newtonian Fluid Mech. 1977, 2: 353-365.
- [4] N. Phan-Thien, A non-linear network viscoelastic model, J. Rheo. 1978, 22(3): 259-283.
- [5] B. Debbaut, Non-isothermal and viscoelastic effects in the squeeze flow between infinite plates, J. Non-Newtonian Fluid Mech. 2001, 98(1): 15–31.
- [6] J. D. Sherwood, Model-free inversion of squeeze-flow rheometer data, J. Non-Newtonian Fluid Mech. 2005, 129(2): 61-65.
- [7] J. H. Kim and K. Hyun, A new instrument for dynamic helical squeeze flow which superposes oscillatory shear and oscillatory squeeze flow, Rev. Sci. Instrum. 2012, 83(8): 085105(1-8).
- [8] D. Cheneler, J. Bowen, M.C.L. Ward, M.J. Adams, Micro squeeze flow rheometer for high frequency analysis of nano-litre volumes of viscoelastic fluid, Microelectronic Engineering 2011, 88(8): 1726-1729.
- [9] D. Cheneler, The Design and Analysis of a Micro Squeeze Flow Rheometer, Ph.D. Thesis, Department of Mechanical Engineering, University of Birmingham, UK, 2010.
- [10] R. G. Larson, A critical comparison of constitutive equations for polymer melts, J. Non-Newtonian Fluid Mech. 1987, 23(87): 249-268.

- [11] M. Aboubacar, H. Matallah, M.F. Webster, Highly elastic solutions for Oldroyd-B and Phan-Thien/Tanner fluids with a finite volume/element method: planar contraction flows, J. Non-Newtonian Fluid Mech. 2002, 103(1): 65– 103.
- [12] A.S. Palmer and T.N. Phillips, Numerical approximation of the spectra of Phan-Thien Tanner liquids, Numerical Algorithms 2005, 38(1-3): 133-153.
- [13] W. Cao, C. Shen, C. Zhang et al, Computing flow-induced stresses of injection molding based on the Phan–Thien–Tanner model, Archive of Applied Mechanics 2008, 78(5): 363-377.
- [14] Y. Kobayashi, Y. Otsuki, H. Kanno, Y. Hanamoto, T. Kana, Crystallization of Polypropylene Near the Surface in Injection-Molded Plaques: A Comparison of Morphology and a Numerical Analysis, POLYM. ENG. SCI. 2011, 51(7): 1236–1244.
- [15] O. James, On the Formulation of Rheological Equations

- of State, Proceedings of the Royal Society of London. Series A, Mathematical and Physical Sciences 1950, 200: 523–541.
- [16] M. I. A. Othman, N. H. Sweilam, Electrohydrodynamic instability in a horizontal viscoelastic fluid layer in the presence of internal heat generation, Can. J. Phys. 2002, 80(6): 697–705.
- [17] M. I. A. Othman, Electrohydrodynamic stability in a horizontal viscoelastic fluid layer in the presence of a vertical temperature gradient, Int. J. Eng. Sci. 2001, 39(11): 1217-1232.
- [18] M. I. A. Othman, M. A. Ezzat, Electromagneto-hydrodynamic instability in a horizontal viscoelastic fluid layer with one relaxation time, Acta Mechanica 2001, 150(1-2): 1-9
- [19] J. N. Sharma, R. Chand, M I. A. Othman, On the propagation of Lamb waves in viscothermoelastic plates under fluid loadings, Int. J. Eng. Sci. 2009, 47(3): 391-404.



#### Journal of Mechanical Engineering Research

http://ojs.bilpublishing.com/index.php/jmer



#### **ARTICLE**

# Finite Element Analysis of Stuffing-box Packing Subjected to Thermo-mechanical Loads

#### Kaoutar Bahoum\* Mohammed Diany Mustapha Mabrouki Jaouad Azouz

Faculté des Sciences et Techniques, Laboratoire Génie Industriel, Mghila, BP. 535, Beni Mellal, 23000, Morocco

#### ARTICLE INFO

#### Article history:

Received: 24 October 2018 Accepted: 10 December 2018 Published:28 December 2018

#### Keywords:

Finite element method

Gland stress Stuffing box Temperature

#### ABSTRACT

The principal rule for the stuffing-box packings is to ensure the stem valve sealing. The behavior of these systems is affected by the operating conditions, which are the gland axial stress, the temperature, and the fluid pressure, as well as the mechanical and geometrical properties of the various components. In this paper, a numerical study using finite element method is presented to evaluate the radial contact stresses, the axial stresses, and the lateral pressure coefficients in a stuffing box system under the tightening gland load and the temperature field. The results of the elaborated numerical model show that if the temperature of the confined fluid varies, the contact pressures and the lateral pressure coefficients vary accordingly. When the temperature of the fluid increases, the tightening stress must be adjusted to ensure leak tightness and thus efficiency and efficiency of the gland system.

#### 1. Introduction

The packed stuffing boxes are the most systems, designed for sealing, used in the industrial installations. Their role is to ensure sealing of stemvalve, piston pins, and actuators. They stop the fluid confined inside an equipment escape to outside. Braided packing rings, made from deformable and relatively incompressible materials, are compressed to perform this sealing function. The malfunctioning of these assemblies can cause considerable damage to the environment and in some cases life losses. The braided gaskets are com-

pressed by the gland; between the stem and the housing; as shown in Fig.1.

The application of optimum gland axial stress generates contact pressures at packing-housing and at the stem-packing surfaces. The optimum value of this contact pressure is required to ensure the effectiveness and efficiency of the confinement. The confinement of fluid is also, affected during operation by temperature. The transfer of heat from the confined fluid to the components of the assembly has not yet been integrated into the design and modeling of gland assemblies with braided seals.

Kaoutar Bahoum

Faculté des Sciences et Techniques, Laboratoire Génie Industriel, Mghila, BP. 535, Beni Mellal, 23000, Morocco

 ${\it Email: bahoum.kaoutar@gmail.com}$ 

<sup>\*</sup>Corresponding Author:

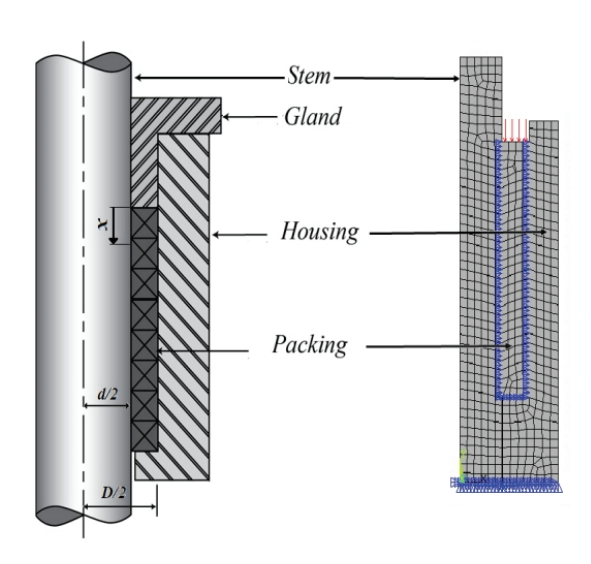


Figure 1. A packed stuffing-boxing system

The stresses distribution in stuffing-box systems attracted considerable attention from researchers over the past few decades. During the installation of the stuffing-box systems, the tightening of the gland imposes a non-uniform distribution of the axial pressure along the packing. A substantial portion of this axial stress is transferred to the stem and the housing through the side surfaces of the packing as a contact pressure. Older studies [1] have shown that these stresses vary exponentially according to the axial position as mentioned in the expression in equation (1).

$$\sigma_{x} = \sigma_{D} e^{-\beta x}$$

$$q_{i} = K_{i} \sigma_{D} e^{-\beta x}$$

$$q_{o} = K_{o} \sigma_{D} e^{-\beta x}$$
(1)

With D the axial stress applied by the gland to the upper packing surface.  $q_i$  and qo are radial contact stress at the packing-stem and the packing-housing interfaces.  $K_i$  and Ko are the lateral pressure coefficient at the packing-stem and the packing-housing interfaces, which represents the transfer rate of the axial stress in radial stress, and a coefficient characterizing the materials and the geometry of the assembly components.

The first expression of noted $_1$  is proposed by Ochonski  $^{[1]}$  considering the equilibrium of forces acting on the packing. The second expression, noted 2, is calculated by Pengym et al $^{[2]}$ , adding the balance of moments but always keeping punctual forces. The third expression, noted  $b_3$ , is proposed by Diany et al. $^{[3]}$ , considering a uniform distribution of the contact stresses. Equation (2) presents the three expressions of b.

$$\beta_1 = \frac{4(\mu_i K_i d + \mu_o K_o D)}{D^2 - d^2}$$

$$\beta_2 = \frac{16(\mu_i K_i d - \mu_o K_o D)}{(D - d)^2}$$
 (2)

$$\beta_3 = \frac{24(\mu_i K_i d - \mu_o K_o D)}{(D - d)^2}$$

Where d and D are the inner and outer packing radii (mm),  $\mu_i$  and  $\mu_o$  are the Friction coefficient between packing-stem and between packing-housing respectively.

The behavior of the packing in the operating conditions relative to its axial compression, which produces radial contact stresses, is characterized by the factors K<sub>i</sub> and K<sub>o</sub>. The determination of these key factors was initiated experimentally by Bartonicek et al. [4-5], and Klenk et al. [6-7]. Thereafter, Diany et al. [8] proposed a simplified analytical approach using the thick-walled cylinder theory to study stresses and displacements of stuffing-box packing and calculate the lateral pressure coefficients. They proved that the contact pressure ratio is approximately equal to one and that the interface contact pressure depends on different parameters such as the assembly geometry, friction and the mechanical characteristics of the used materials. The same authors [9] developed a hybrid method to characterize the braided packing. Three-axial compression tests combined with finite element simulations were used to evaluate lateral pressure coefficients, elasticity modulus, and Poisson's ratio. They calculated these characteristics for Teflon and flexible graphite packings.

Kazeminia et al. [10-12] presented several analytical models to evaluate the stresses in the stuffing-box components. They presented a contact stress modeling study based on two configurations. The first configuration consists to introduce a variable gap between the packing and the housing in order to create a uniform axial stress distribution. The second configuration consists of inserting one ring of the gasket at a time and using the loading and unloading process to create plastic deformation and residual stresses. They also developed an analytical model based on the combination of ring theory, thin cylinder theory, and beam on elastic foundation theory. The results of the analysis approaches were compared with finite element analysis and experimental tests results.

The temperature influence has not been introduced to date in analytical models. Only a few experimental works have dealt with this influence on stuffing-box packings. Veiga et al. [13] and Girao et al. [14] presented experimental studies; they evaluated the packings expansion under different temperatures and their influence on stresses. These tests show that the packing expansion, due to temperature

variation, increases the applied compressive gland load. The results indicate also that if the volumetric content of packing material is higher, the gland stress increases and the leakage control becomes more difficult.

The purpose of this work is to evaluate the effect of the confined fluid temperature on the distribution of axial stresses, contact pressures, using 2D finite element model of the packed stuffing box. The variation of the lateral contact pressure coefficients is also examined.

#### 2. Finite Element Analysis

The study and the modeling of the mechanical assemblies are carried out either by the exploitation of analytical models developed after an accumulated expertise over a long period or by numerical modeling ensured with the help of commercial software more or less sophisticated. A third way is an experimentation either by creating a test bench or by monitoring the actual equipment in the operating sites. In packed stuffing-box case, the study of the temperature effect on mechanical behaviour and leakage is not yet taken into account in the analytical models developed to date. Therefore, a first attempt, using numerical analysis, will certainly allow ground preparation for future analytical studies to consider the temperature effect. In this work, a finite element model, using Ansys software [15], is proposed to evaluate the behaviour of the stuffing box packing assembly subjected to combined loads: clamping force applied by the gland and thermal conditions representing the operating environment.

#### 2.1 Finite Element Model

The stuffing-box with hyperelastic packings is composed of four elements: the stem, the packings, the housing and the gland. All components have a cylindrical symmetry. This nature of symmetry, as well as the symmetry of the mechanical load and the boundary conditions reflecting the temperature distribution, allowed working with a simple axisymmetric model in 2D. This axisymmetric model is used to study the combined effect of the fluid temperature and the compression load on the axial distribution of the contact pressure and the lateral pressure coefficients, at the stem-packing and the packing-housing interfaces.

Figure 1 shows this model with the obtained mesh. A2D element with eight nodes, PLANE223, with four degrees of freedom per node (three displacements and temperature), is chosen for this study. The assembly components are in the radial direction contact. Contact elements are used to simulate the reaction of the stuffing-box elements when they are in contact. The elements CONTA172 and TARGE169 are used.

#### 2.2 Materials Characteristics

The mechanical properties of the Stuffing-box compo-

nents affect the resulting stresses and displacements. In this study, the stem and the housing are made of ordinary steel and the braided packing is made of Polytetrafluoroethylene (PTFE). Table 1 shows the mechanical and geometrical properties of the assembly components.

**Table 1.** Stuffing-box components material properties

	Stem	Packing	Housing
Inner radii (mm)	-	14.29	23.89
Outer radii (mm)	14.29	23.89	33.75
Young Modulus (GPa)	200	0.126	200
Poison's coefficient	0.3	0.4	0.3
Coef. of thermal Exp. K <sup>-1</sup>	11.6E-6	126E-6	11.6E-6

#### 2.3 Boundary Conditions

The boundary conditions must represent the real operating conditions. Effectively, the upper surface of the packing is subjected to uniform axial compression load representing the clamping load applied by the gland. The lower surfaces of the housing and the stem are at a uniform high temperature transferred from the confined fluid. The other outer surfaces are at room temperature. The radial and axial displacements are blocked at the bottom of the assembly.

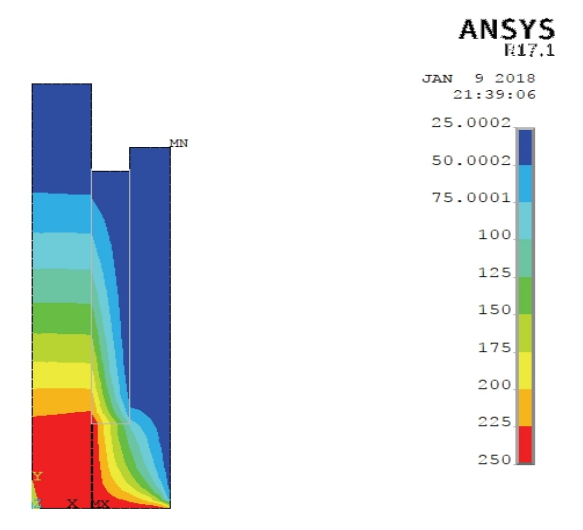
The radial contact pressures, the axial stresses and the lateral pressure coefficients under different temperature configurations and tightening load, are examined.

#### 3. Results and Discussions

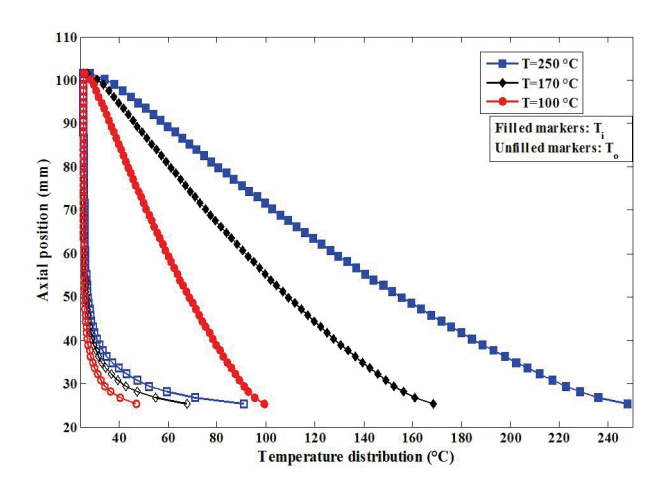
The results of previous studies show that the mechanical and geometrical characteristics of the packed stuffing-box components, as well as the loading conditions, have an influence on the values of the stresses and deformations. To evaluate the effect of the fluid temperature, as a new parameter, on the distribution of stresses and the coefficients characterizing the materials and geometrical proprieties of the assembly components, the axisymmetric model presented in the previous paragraph is implemented. For many axial tightening loads, different values of the fluid temperature have been adopted. The chosen values reflect the actual operating temperature range of the stuffing-box packings.

Figure 2 shows the temperature distribution in the stuffing-box assembly when the fluid temperature is about 250 °C. At the bottom of the housing, the temperature is imposed; it corresponds to the fluid one. The other walls of the system are at room temperature.

More detailed temperature distributions at the inner and outer interfaces of the packing are presented in Figure 3, for three different fluid temperatures. The thermal boundary conditions applied to the assembly causes a non-uniform temperature distribution in the two packing interfaces. At the same axial position, the difference in temperature between the two interfaces is greater when the fluid temperature is higher. This difference increases when the axial position is closer to the lower packing surface.



**Figure 2.** Distribution of temperature in stuffing-box packing



**Figure 3.** Distribution of the temperature in the inner and outer interfaces of the packing

The stuffing box packing ensures the sealing by avoiding the fluid exit towards the external environment. This role is guaranteed by the generation of contact pressures at the stem-packing and packing-housing interfaces. The studies performed at room temperature show that the contact pressures distribution is exponential <sup>[1]</sup>; this is confirmed in figure 4. Actually, when the temperature imposed everywhere is 25°C, the stresses qi and qo are equals and their values increase when the tightening load

increases or when the axial position approaches the packing upper surface.

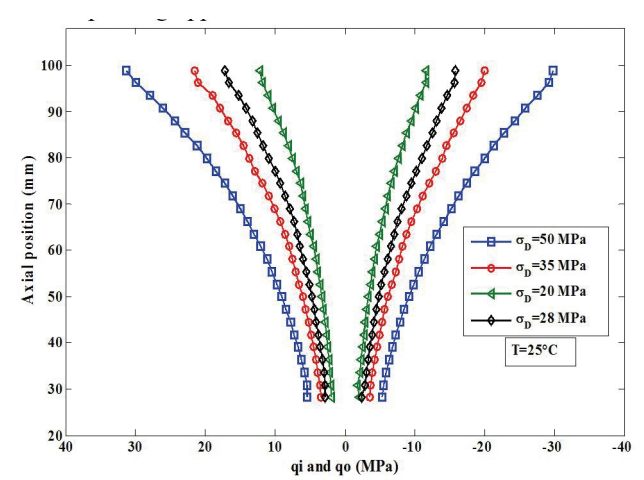
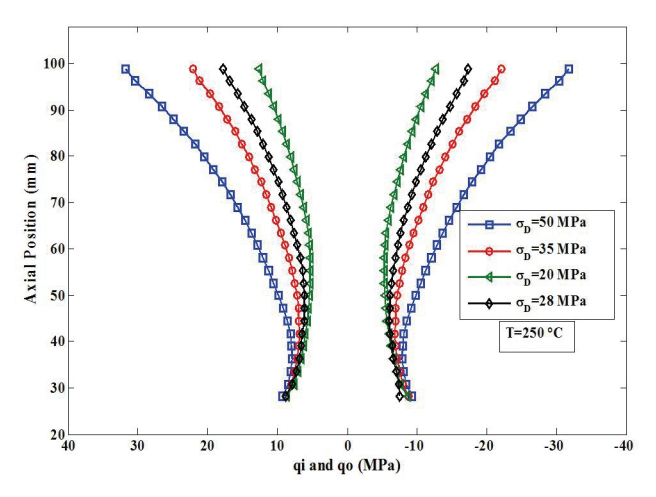


Figure 4. Distribution of radial contact stresses at T=25°C

When the fluid temperature is greater than the ambient temperature, the shape of the stress curves moves away from the exponential form. Indeed, in Figure 5 where the fluid temperature is 250°C, the contact pressures have the same value at the bottom packing surface while the clamping force is different.

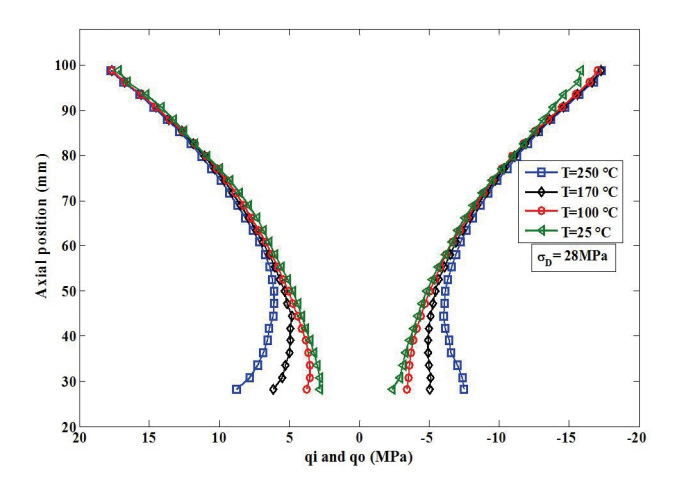


**Figure 5.** Distribution of radial contact stresses at T=250°C

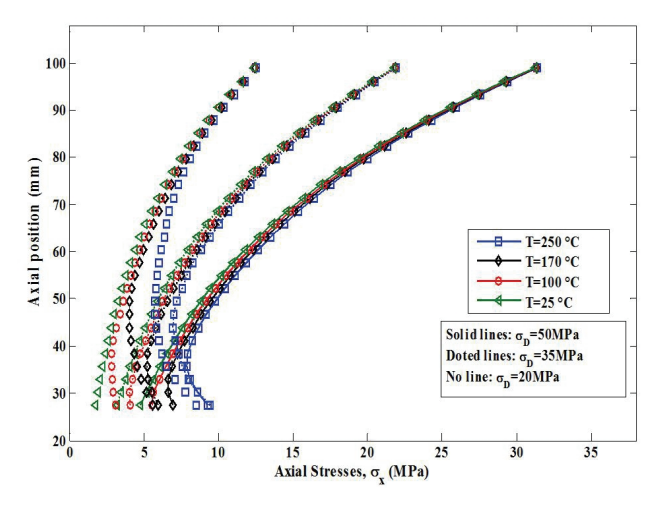
To evaluate the influence of the fluid temperature on the contact pressures, Figure 6 shows the distribution of these stresses for different values of the fluid temperature. The packing upper surface is at the same pressure since it is the same clamping force for all presented cases. The curves corresponding to the different temperatures diverge from an axial position, which depends on the value of the clamping load.

Figure 7. shows the axial stresses distribution at medium diameter of the packing for different temperatures and

gland stress values. The same remarks and conclusions made during the analysis of the other stresses remain valid for these axial stresses.



**Figure 6.** Distribution of radial contact stresses for  $\sigma D$ = 28 MPa



**Figure 7.** Distribution of Axial stresses at the medium diameter of the packing for different temperatures and gland stress values

The stresses expressed in equation (1) are defined by the  $\beta$  coefficient of the exponential form, the clamping load,  $\sigma_D$ , and the coefficients of lateral pressure, Ki and Ko. The main remark announced during the interpretation of the different curves and the question if the exponential form of the stresses distributions is verified or not. To answer this question, the value of the  $\beta$  coefficient is calculated for all the cases studied and the correspondence rate between the EF curves and the exponential form is by specified. Figure 8 gives the variation of  $\beta$  as a function of the fluid temperature for different clamping loads. Figure 9 shows the compatibility ratio between EF data and equation (1). At room temperature, the  $\beta$  coefficient

has the same value for all clamping loads, which confirms the independence of the lateral pressure coefficients of the clamping load at ambient temperature. However, when the fluid temperature is taken into consideration, the value of  $\beta$  changes as a function of temperature and clamping load. In fact, the value of  $\beta$  decreases as the temperature increases or the clamping load decreases. On the other hand, the correspondence rate of the EF curves and equation 1 decreases as the temperature increases or when the clamping load is low. Thus, the exponential shape of the axial distribution of the axial and radial stresses is affected by the fluid temperature consideration. Therefore, it is clear that the lateral pressure coefficients depend on the fluid temperature value and the clamping load.

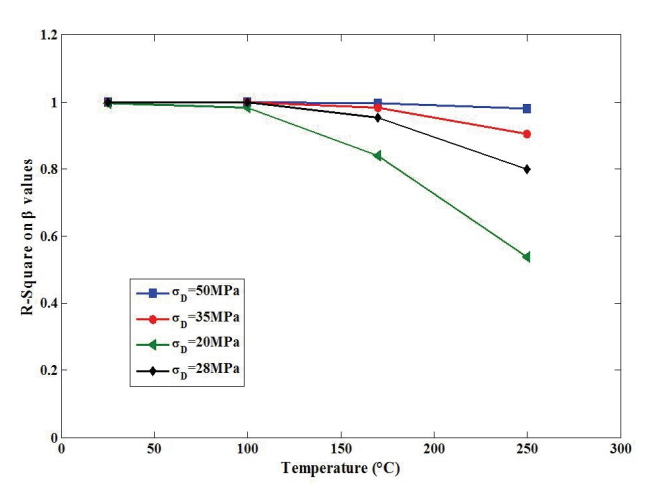
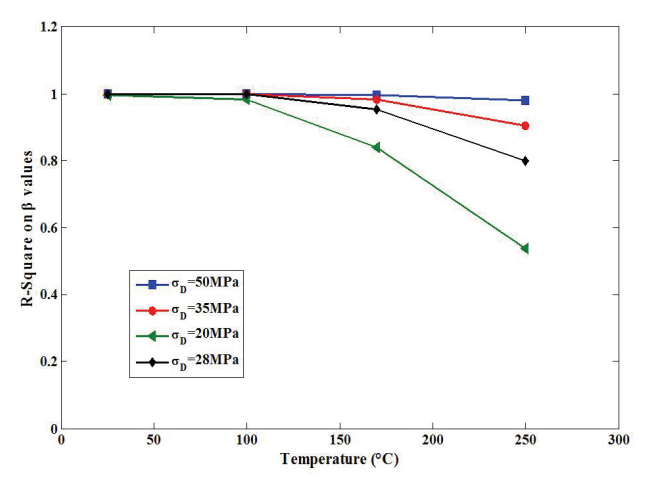


Figure 8. Variation of coefficient  $\beta$  as function of the fluid temperature and different gland stress



**Figure 9.** Compatibility ratio between EF data and equation (1) as function of the fluid temperature and different gland stress

Figures 10 and 11. show the lateral pressure coefficients at the stem-packing interface, Ki, and at the pack-

ing-housing interface, Ko, respectively. In an ambient temperature, the shape of the curves is close to the curve theoretically calculated by Diany and Bouzid [8]. When the temperature increases, the value of Ki does not vary significantly and remains around 0.7. On the other hand, Ko changes enormously and even exceeds the unit, which is supposed to be the theoretical maximum value. This last remark obliges us to reconsider the definition of the lateral pressure coefficients to take into account the temperature effect.

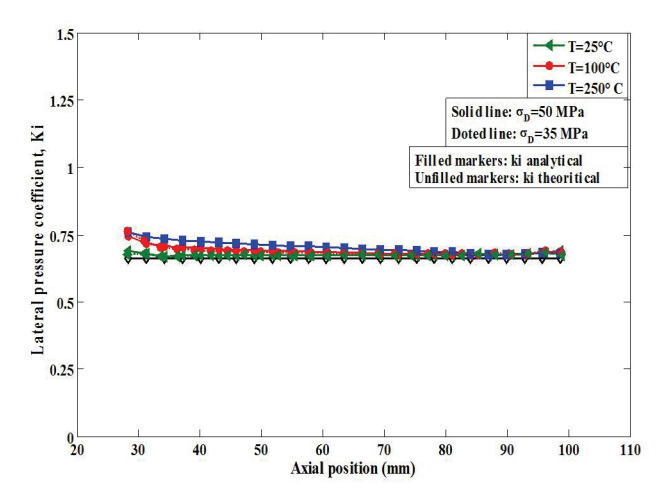


Figure 10. Lateral pressure coefficient Ki

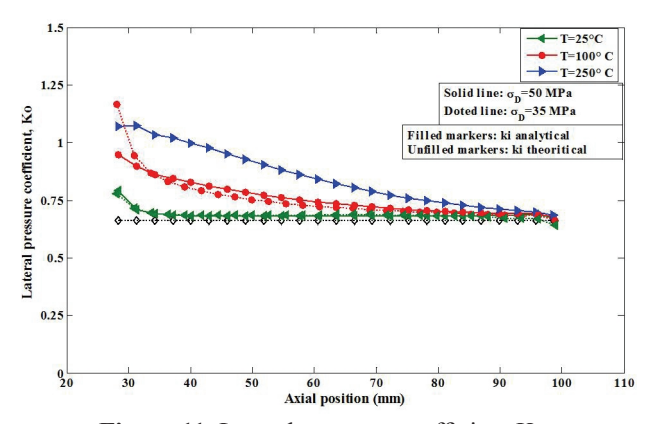


Figure 11. Lateral pressure coefficient Ko

#### 4. Conclusion

The finite element model of the gland assembly under the combined effect of temperature and tightening load is presented. The results of this elaborated numerical model show that:

The variation of the temperature of the confined fluid influences the contact pressures and the axial stresses distributions. Indeed, for the ambient temperature, the stresses shapes respect the equation (1), and when the temperature increases, the curves move away from the exponential form expected in theoretical studies.

The definition of the lateral pressure coefficients should be reconsidered to take into account the temperature effect

The tightening load must be adjusted when the fluid temperature increases in order to ensure leak tightness and the efficiency of the system.

All these finite element analysis conclusions must be compared and validated with analytical and experimental studies.

Nomenclature:

 $\sigma_x$ : Axial stress distribution in the packing, (MPa)

 $\sigma_D$ : Gland axial stress (MPa)

*X*: Axial position (MPa)

 $k_{i,.}$   $k_{o:}$  Lateral pressure coefficient between packing-stem and between packing-housing respectively

 $\mu_{i}$ ,  $\mu_{o}$ . Friction coefficient between packing-stem and between packing-housing respectively

 $q_{i}$ ,  $q_{o}$ . Radial contact stress at the packing-stem interface and at the packing-housing interface respectively (MPa)

d.D. The inner and outer packing radii (mm)

 $\mu i$ ,  $\mu o$ : The Friction coefficient between packing-stem and between packing-housing respectively.

T: Celsius temperature scale

#### References

- [1] Ochonski, W., "Radial Stress Distribution and Friction Forces an a Soft-Packed Stuffing-Box Seal," Tribology International, 1988, 21(1), 31-38.
- [2] Pengyun S., Kuangmin C. and Zongyun D., "A Theoretical Analysis of the Lateral Pressure in a Soft Packed Stuffing Box Seal," Tribology International, 1997, 30(10), 759-765.
- [3] Diany, M. and Bouzid, A,-H. Evaluation of contact stress in stuffing box packing. In: 2006 ASME-PVP conference, paper no. PVP2006-ICPVT11-93083, Vancouver, Britisg Columbia, 2006.
- [4] Bartonicek, J., and Schoeckle, F., "Approach to a Correct Function of Stuffing Boxes," 1996 Computer Technology: Applications and Methodology, ASME, New York,1996, 326, 115–121.
- [ 5 ] Bartonicek, J., and Schoeckle, F., "Tightness and Accurate Mounting of Bolted Joints," 1996 Computer Technology: Applications and Methodology, ASME, New York, 1996, 326, 171–178.
- [6] Klenk, T., Kockelmann, H., Roos, E., Bartonicek, J., and Schoeckle, F., "Characteristics and Testing Techniques for Stuffing Box Packings," ASME Pressure Vessels and Piping Conference, 1999, 382, 135–143.
- [7] Klenk, T., Kockelmann, H., Hahn, R., and Roos, E., "High Grade Proof for Gaskets According to TA-Luft and VDI 2440," ASME Pressure Vessels and Piping Division Conference, 2001, 416, 163–167.

- [8] Diany, M., and Bouzid, A., "Analytical Evaluation of Stresses and Displacements of Stuffing-Box Packing Based of Flexibility Analysis," Tribol. Int., 2009, 42 (6), 980–986.
- [9] Diany, M. and Bouzid, A,-H. An Experimental– Numerical Procedure for Stuffing Box Packing Characterization and Leak Tests. ASME Journal of Tribology, 2011, 133(1).
- [10] Kazeminia, M. and Bouzid, A.-H. Analysis of stresses and strains in packed stuffing-boxes. In: Proceedings of the ASME Pressure Vessels and Piping Conference (PVP '14), Anaheim, Calif, USA, 2014, 1–11.
- [11] Kazeminia, M. and Bouzid, A.-H. Analytical and numerical evaluation of the axial stress distribution of two softpacked stuffing-box configurations. In: Proceedings of the ASME Turbo Expo 2014, Turbine Technical Conference

- and Exposition, D"usseldorf, Germany, 2014, 1–8.
- [12] Kazeminia, M. and Bouzid, A.-H. Stress analysis of packed stuffing-boxes. Journal of Pressure Vessel Technology, 2015, 137, 5.
- [13] Veiga, J. C., Carmo, A. S. and Girao, C. D. The influence on the stuffing box of the forces generated by packing thermal expansion. In: Proceedings of the Pressure Vessels Piping Division Conference (ASME '11), Baltimore, Md, USA, 2011, 227–233.
- [14] Girao, C. D. and Guenther, K. Evaluation of stuffing box forces associated with the thermal expansion of e-PTFE and graphite packing sets. In: Proceedings of the ASME Pressure Vessels and Piping Conference, Toronto, Canada, 2012, 167173.
- [15 Ansys. Standard Manuel. Version 17.1.



#### Journal of Mechanical Engineering Research

http://ojs.bilpublishing.com/index.php/jmer



#### **ARTICLE**

# Some Aspects of Fretting Fatigue under Complex Cyclic Contact Load Condition

#### Farshad Abbasi

Mechanical Engineering Department, Faculty of Engineering, Bu-Ali Sina University, Hamadan, Iran

#### ARTICLE INFO

#### Article history:

Received: 25 October 2018 Accepted: 10 December 2018 Published: 28 December 2018

Keywords:
Fretting Fatigue
Wear
Cyclic normal load
Tribology
Al7075-T6
Contact mechanics.

#### ABSTRACT

Fretting fatigue has been studied mainly under constant normal loading, as it requires simple equipment which can be assembled on a universal fatigue testing machine. Recently, the authors<sup>[1-3]</sup> have introduced an innovative fretting fatigue apparatus in which the contact pressure can independently be varied during the test. It was found that the low frequency of normal load has drastic effect on fretting fatigue life. The authors have compared the results of constant normal loading with those of in phase, 90° and 180° degrees out-of-phase loadings. The case of constant normal load is found to be the least damaging, while the inphase loading is found to be the most damaging. When load is varied in phase with the axial stresses in the specimen, contact mechanics would predict that no slip should be obtained, whereas apparently larger slip is found with respect to the constant normal load. When loads are out-of-phase, the "full sliding limit" is also time-varying and less frictional force is developed so it becomes hard to interpret why life is nevertheless shorter than in the case of constant normal load. Hence, the objective of this article is to present further discussion of the experimental results. The authors hope that this discussion could lead to some progress.

#### 1. Introduction

ost of the previous studies on fretting fatigue, have been accomplished under constant normal loading and a less attention has been paid to the effects of cyclic normal loading. One of the most important issues with rareness of investigations under cyclic normal loads is the difficulties associated with design

and manufacturing the apparatus capable of simulate such complex load conditions. Recently [1] the authors have developed a new electromechanical test-rig to investigate the fretting fatigue behavior of material under cyclic contact loads.

Examination of fretting scars using optical microscopy, SEM and EDS revealed that the abrasive wear of debris

Farshad Abbasi

Mechanical Engineering Department, Faculty of Engineering, Bu-Ali Sina University, Hamadan, Iran Email: farshadabbasi788390@gmail.com

<sup>\*</sup>Corresponding Author:

particles and higher oxidation rate due to the normal load release at each cycle, severe delamination of the wear particles and the dominant partial slip condition with wider slip region compared to constant normal loading, are the most important reasons for significant reduction of fretting fatigue life, under cyclic normal loading, especially for low normal load frequencies <sup>[2,3]</sup>. Huq et al. <sup>[4,5]</sup> Hojjati-Talemi et al al. <sup>[6]</sup> Xin et al. <sup>[7]</sup> found that the presence of cyclic normal loading condition reduces fatigue lifetime drastically. Madge, et al. <sup>[8]</sup> simulated fretting fatigue using FEM, taking into account wear and concluded that the dominant mechanisms in gross slip and partial slip condition are wear and cracking, respectively.

Vingsbo and Soderberg [9] introduced a fretting map shown in Figure 1 and showed that as the tangential displacement amplitude increases, the wear rate increases, the partial slip regime dominates and the fatigue life reduces. Maximum damage occurs at relative tangential displacement amplitudes within the range of 10-20 microns. This map has been later found to give an erroneous interpretation in some cases [10]. Although, the Vingbo and Soderberg map [9] proposed 30 years ago was a significant step forward in the fretting fatigue context at the beginning but with the ever increasing progress in the this area, the map gradually lost its accuracy. For example, the range of 10-20 microns for tangential displacement that causes the maximum damage is not fully accurate and globally accepted and depends on the test equipment design. It has also been found that in general, the range of tangential displacement depends on contact type, specimen geometry, load and material.

More recently, Ciaverella et al [11] has proposed a simplified extension of the Crack Analogue (CA) model assuming Half-Space condition for fretting fatigue with varying normal load. They provided a very interesting approach to model the fretting fatigue situation as a crack or notch. This approach was first suggested by Giannakopoulos et al. in 1998 [12] arguing that the stress field created near the contact pad is similar to that created ahead of a sharp crack. If this Crack Analogy (CA) can be made, then it might be possible to predict the behavior in the contact problem by finding an equivalent crack. The first limitation of this model is that, in the real applications where these conditions are not met, half-plane theory cannot be applied for the solution of the problem. A second difficulty with this approach is that tribological features of the contact interface is not considered in their model. Crack initiation and consequently fretting fatigue lifetime is affected not only by the contact stresses but also by the localized surface damages and tribological features (fretting regime) of the contact interface. Unlike the constant normal load condition, in variable normal loading the normal load is released in each cycle exposing periodically the fretting area to more oxidation. Under oxidizing conditions, cracking and delamination of the wear particles will be accelerated by oxidation of the particles.

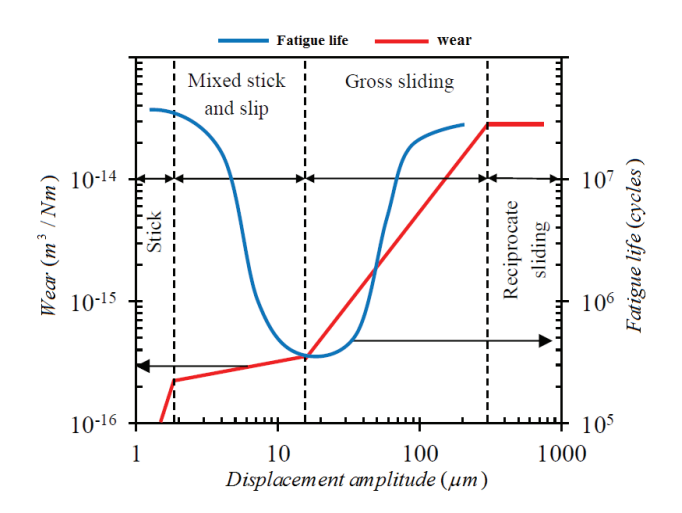


**Figure 1.** Schematic view of the fretting map [9]

Oxide debris forms at contact interface, acting as abrasive particles and are pushed into the fatigue crack as the process continues. ASTM International defines abrasive wear as the loss of material due to hard particles or hard protuberances that are forced against and move along a solid surface [13]. Waterhous et al [14] believes that if the oxide layers are harder than the base material, fretting damage and crack initiation are accelerated. On the other hand, if the oxides are soft relative to the base material, it lowers friction and fretting damage reduces significantly. The detached particles are generally trapped between the contacting surfaces and subsequently are crushed into smaller fragments by the mechanical action of fretting. Because the oxides are usually harder than the underlying metal, the fragmentation will be enhanced by oxidative conditions, especially in the case of cyclic normal load. In the slip region, the fragmented particles will roll between the surfaces causing grooving damage until they finally, leave the contact area.

Recently, Ciaverella [15] has published a discussion on author's publications [1-3]. He believes that some of the experimental results don't conform to the existing theories and requested a discussion on the results. Therefore, the objective of this article is to answer three main points he has raised in [15], in the hope that this discussion could lead to some progress.

#### 2. Features and Considerations

The interplay of fretting fatigue and wear has remained largely unexplained and particularly the region when

tangential displacements are above the gross sliding conditions where it is unclear why a large improvement of fatigue live is observed in fretting maps, despite wear is not so largely increased. Hence, further discussion of the experimental results is needed and is the main objective of present study. With this state of affair, it is quite naive to expect very detailed predictions of fretting fatigue to be possible, given we have in one go the uncertainties typical of fatigue problems, of tribological prediction of friction coefficients and its evolving in time, the wear problem, and the interplay of all of them at the same time. In the case with cyclic normal load condition, the frequency of normal contact load is the most important parameter because it interacts with several parameters (e.g. contact stresses, friction force, oxidation rate, slip amplitude etc.) and influences the fretting fatigue behavior. In this section, the effects of frequency on fretting fatigue response and tribological behavior of contact interface is presented in details.

#### 2.1 Frequency and Slip Regimes

The major drawback of this kind of loading in the newly designed fretting apparatus [1] is that the frictional forces are dependent on the axial strain in the dog bone specimen and on the stiffness of the bridge type fretting pad. Therefore, by oscillating the normal load in-phase with the axial load, the level of frictional load also varies accordingly. This means that by introducing cyclic normal load the level of frictional forces becomes an extra variable, hence true contact stresses and overall fatigue load changes accordingly. Let's consider the case where normal load is constant. In full stick conditions, the tangential friction force increases in-phase with specimen elongation until gross sliding occurs while the contact stresses increases at the same time. On the other hand, if normal load oscillates between zero and preset maximum value (in-phase condition), then the situation is different. When normal load is zero, then tangential forces will be zero also. Depending on the normal load frequency, with respect to the bulk stress frequency, limitations will be applied to the magnitude of tangential friction load. If the normal load frequency is very large, then the maximum friction force amplitude will be about the same than in the case of constant normal load, although the stress history will be different. When the normal load frequency is low, the tangential friction forces is released alternatively when the normal load reduces to its lowest level and there will be no net friction force at all. This is confirmed by the numerical simulation shown in Figures 2 and 3 in which shear stress increases and slip region decreases with the increase in contact load frequency.

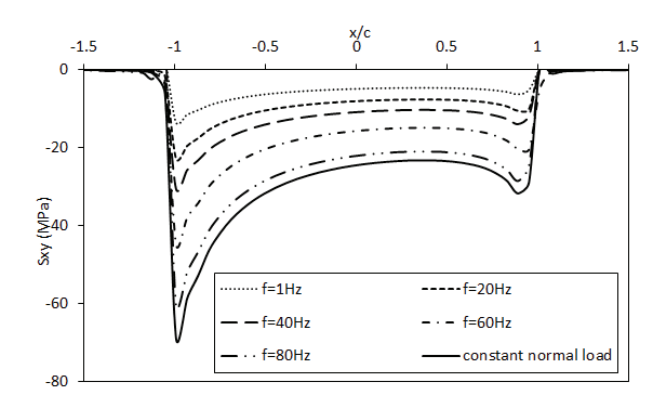


**Figure 2.** Shear stress distribution along the contact interface [2]

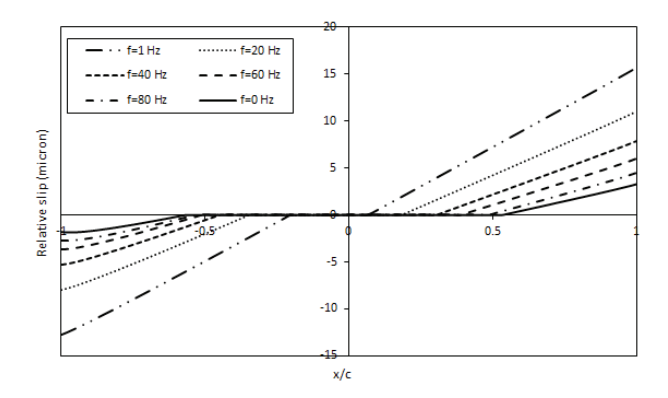


**Figure 3.** Relative displacement distribution along the contact interface [2]

Let's explain further why shear stresses in the case of constant normal load is higher than cyclic one. The loading sequence for both the constant and in-phase cyclic contact load conditions for one cycle with the time period of T is depicted in Figure 4. As it is seen, the axial load is the same for both the constant and cyclic contact loading conditions. However, the contact load for cyclic loading conditions is always (except at T/2 where the contact load is the same for both loading conditions) lower than that for the constant loading condition. Therefore, the shear stress due to the contact load and friction will be higher in constant loading conditions. Since, the shear stresses affecting the slip region depends on the history of loading, less effective shear stress and subsequently larger slip zone is expected for the case of cyclic normal contact loading.

The fretting fatigue behavior (and hence the resulting stresses and displacements in the contacting bodies) and also tribological condition of the contact interface depends on the history of loading. Therefore, as expected, at very low normal load frequencies the contact interface experiences less average amount of frictional stresses with respect to those in constant normal load where the normal

load is maximum at all axial load cycles. In the case with high normal load frequency, the number of points in the load cycle in which the normal load is maximum increases and the condition of contact interface, tends to the conditions of the constant contact loading, thus further average normal load is expected to apply on the contact interface. As a result, having the same axial load, higher frictional resisting force and subsequently lower tangential displacement occurs on the contact interface.

The authors think that this explains partly (i) why slip size for in-phase loading is larger than that for constant normal load and (ii) why slip size decreases and fatigue life increases when the normal load frequency is increased, although the presence of cyclic normal load will bring about its own fatigue component.

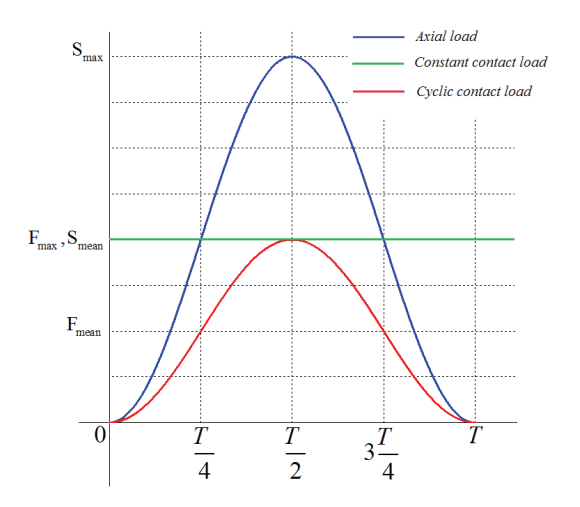


**Figure 4.** Loading sequences for constant and cyclic contact loading

#### 2.2 Frequency and Wear Rate

It should be emphasized that, cyclic normal load tests with load ratio of R=0, induce contact opening at each cycle, so air reaches the fretted interface. As the authors have stated in [2] "At higher contact load frequencies, there is less time for chemical reaction". Here it is necessary to make a distinction between "reaction time" and "opening time". Reaction time is the time during which oxygen reacts with base material in the slip region. Opening time is the time during which the contact is open in each fatigue cycle. Hence, due to the flow of the air and the normal load mechanical mechanism, reaction time is lower than the opening time. At high normal load frequencies, the contact closes immediately at each cycle before the air have chance to reach the wear particles (this is because there is no mechanism to return the pad after it's touching to the specimen). The higher the frequency, the shorter is the time available for chemical reactions to occur. Therefore,

low wear rates can be obtained at high frequencies. However, at low normal load frequencies more oxygen can reach the fretting surface, thus debris are exposed longer to the atmosphere giving rise to a homogenous oxidation over the whole interface. This conclusion has also been reported in several investigations dealing with the effect of normal load frequency on fretting in the literature [16-18].

For more clarification let's consider the case where normal and axial load frequencies are 1Hz and 10Hz respectively as shown in Figure 5. In this case where the normal load frequency is very low, during the time period of 1 second, 10 cycles of axial load is applied for each cycle of normal load. The exposure time (when the contact is open) for one axial load cycle is higher than the closure time (when the contact is closed), i.e. more time for chemical reactions to occur in the contact between the pad and specimen. Now let's consider the case where normal and axial load frequencies are 80Hz and 10Hz, respectively, as shown in Figure 6. In this case, where the normal load frequency is high, during the 0.1 second, 8 cycles of normal load is applied for each cycle of axial load. In this case, the number of points in the load cycle in which the normal load is maximum increases and the condition of contact interface, tends to the conditions of the constant contact loading. In this case, the exposure time for one axial load cycle is lower than that of the closure time, i.e. less time for chemical reactions between the pad and the specimen. Therefore, wear and oxidation occur at lower rates for higher frequencies.

As a matter of fact, the condition of contact interface at high frequencies is very similar to that at constant contact load. This point is more clearly in Figure 7 where the peak points of cyclic normal load forms a line that is tangent to the constant normal load. In this case, the sum of time intervals when the contact is close is higher than those when the contact is open. Therefore, lower oxidation occurs at higher frequencies. The above reason may explain why in Figure 13 in reference [2], the slip area decreases with increase in normal load frequency. This also explains partly why fatigue life increases when the normal load frequency is increased and at f=80Hz it converges to its corresponding life at constant contact load condition.

Other possibilities could be related to the impact like conditions at higher frequencies, local temperature rise at the contact interface, and or changes/transfer of the oxides between the mating surfaces. The contact temperature is a dependent variable, being a function of thermal properties of the contacting bodies as well as size and shape of the real contact area, frequency and sliding velocity, normal load amplitude and coefficient of friction. Temperature may affect the process of fretting because of two reasons:

(i) the mechanical properties of materials change with temperature; (ii) the corrosion and oxidation rates usually increase with temperature. This subject has been neglected in most of investigations and the results given in the literature are controversial.

As a suggestion for future works, more realistic and documentary discussions can be presented by measuring the slip amplitude, exposure time, wear rate, contact interface temperature rise, amount of oxide debris, possible change in COF (coefficient of friction) and providing more meaningful illustrations such as variations between normal load frequency and oxide debris, wear rate and exposure time. These would necessitate that the testing device is equipped with more sophisticated measuring instruments.

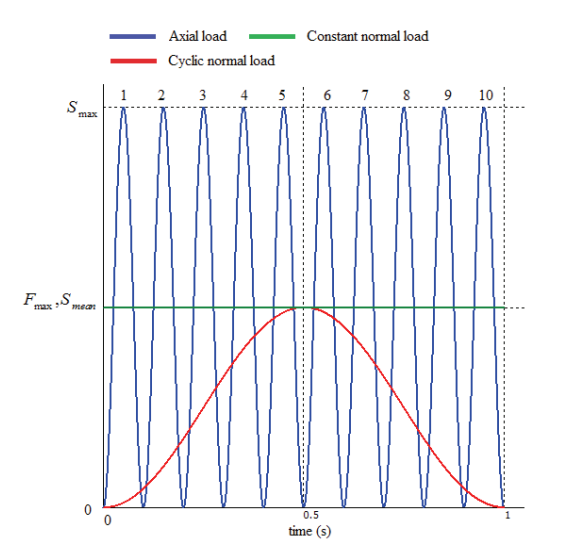


**Figure 5.** Loading sequence for normal load frequency of 1Hz and axial load frequency of 10Hz.

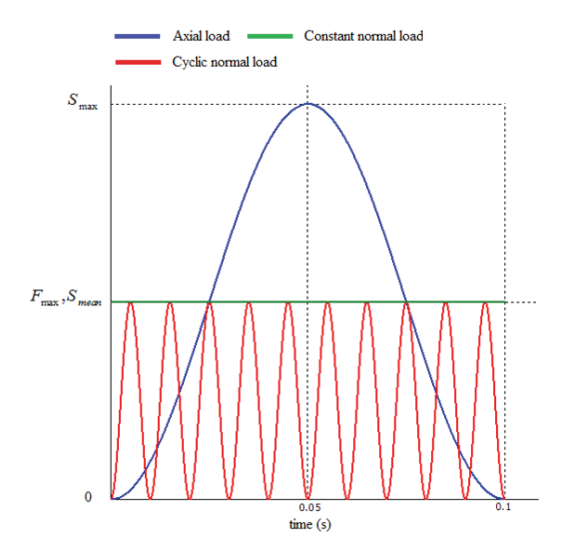


**Figure 6.** Loading sequence for normal load frequency of 80Hz and axial load frequency of 10Hz in time period of 0.1s

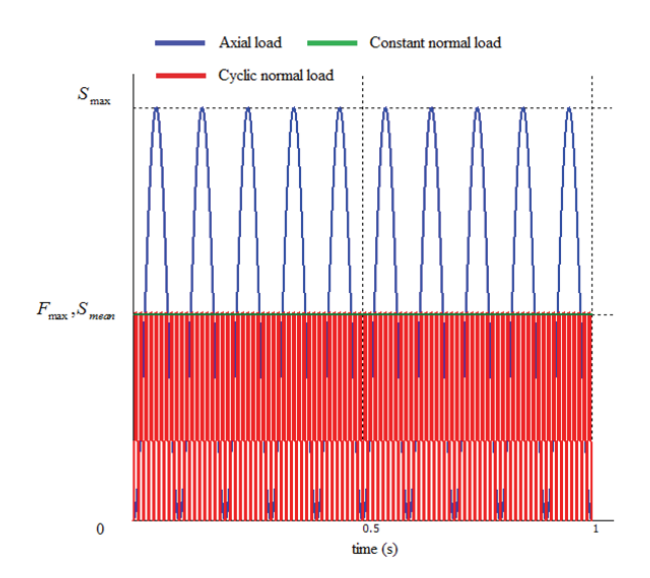


**Figure 7.** Loading sequence for normal load frequency of 80Hz and axial load frequency of 10Hz in time period of 1s

#### 2.3 Tribological Effects

Fretting fatigue and contact mechanics calls for some new models under cyclic normal loading. The main founding of the investigation <sup>[2,3]</sup> was to show that the fretting fatigue life is closely related not only to the contact stresses but also to the tribological behavior of the contact interface and relative tangential displacement of two contacting surfaces. However, these factors are more influential at very early stages of fretting fatigue life i.e. crack initiation phase. The results suggests how difficult is to interpret "fretting fatigue", and even "crack and notch" analogues which do not consider the tribological effects of wear and the change of contact area, can be oversimplified.

Generally, fretting fatigue life could be divided into two main phases, namely crack initiation and crack propagation. The fraction of each phases depends on many factors, e.g. slip regime, load frequency, environmental conditions, contact stresses, axial bulk stress, slip amplitude, etc., and varies from one practical application to another. The initiation process in fretting contact is a mixture of wear, corrosion, and fatigue phenomena. Early attempts to explain the initiation of fretting fatigue cracks were based on stress criteria alone. However, such an approach is bound to fail since the effects of slip amplitude are not taken into account. Therefore, some other parameters such as slip amplitude, which is sensitive to small variation of applied stress, should be taken into account. As stated by Hills and Nowell [19] one of the principal goals of any mechanic's analysis of crack initiation in fretting must be to incorporate the effects of relative slip or displacement amplitude. However, at the present time there is no theory

to model these effects for fretting fatigue life estimation.

#### 3. Final Remarks

Until now, only a few authors have used experiment to study the effect of cyclic normal loading on fretting fatigue life. Moreover, no investigation has so far been performed to assess the influence of normal load frequency and out-of-phase loading on fretting fatigue under cyclic normal loads. The authors believe that, what has been done in [1-3] is only a beginning and needs complementary works to be done in future for eliminating the deficiencies of the work. However, the more complex fretting loading, the more complex fatigue analysis will be. If the cyclic bulk stress and contact loading are applied in a non-proportional manner, much care must be taken when analyzing frictional contacts in partial slip, whether by use of the classical methods or numerical techniques such as finite element analysis (history-dependence may also be important). The authors believe that more investigation (both experimental and analytical) are now required for a better understanding of the fretting fatigue phenomenon under cyclic normal loading including Archard wear modeling, tribo-oxidation processes and damage mechanics analysis. To the best of author's belief, developing a fatigue model considering these effects is necessary to understand fretting fatigue behavior under cyclic normal loading. Furthermore, some simplifications and assumptions have made in the analysis and simulation, as is usual in engineering analysis, for some of which the authors may not have convincing answer. Definitely, there are still many latent aspects which must be clarified in the context of fretting fatigue under fluctuating contact loads. The authors have travelled some of the way but there is a long way still ahead to travel.

#### References

- [1] F Abbasi, GH Majzoobi and MM Barjesteh, Developing a new experimental set up to study fretting fatigue behavior under cyclic contact loading, Proc IMechE Part J: J Engineering Tribology, 2017, 1–14.
- [2] G.H. Majzoobi, F.Abbasi, An investigation into the effect of normal load frequency on fretting fatigue behavior of Al7075-T6, Tribology Transactions, 2017,1-13.
- [ 3 ] Abbasi F, Majzoobi GH. Effect of out-of-phase loading on fretting fatigue response of Al7075-T6 under cyclic normal loading using a new testing apparatus. Eng Fract Mech, 2017. https://doi.org/10.1016/j.engfracmech.2017.08.010.
- [4] Huq M.Z., Butaye C. and Celis J.P.An innovative system for laboratory fretting wear testing under oscillating normal force, 2000, 15 (7), 1591–1599.
- [5] Huq M.Z. and Celis J., Fretting fatigue in alumina tested under oscillating normal load, J. Am. Ceramic Soc 2002,

- 85, 986-988.
- [6] Hojjati-Talemi R., Wahab M.A. and Baets D.P.Finite element simulation of phase difference effects on fretting fatigue crack nucleation behaviour, Proc IMechE Part J: J Eng Tribol. 2014, 228 (4), 470–479.
- [7] Xin L., Jianwei Y., Meihong L. and Zhengxing Z., An investigation on fretting fatigue mechanism under complex cyclic loading conditions, Int J Fatigue, 2016, 88, 227–235.
- [8] Madge J.J., Leen S.B., McColl I.R. and Shipway P.H., Contact evolution based prediction of fretting fatigue life: Effect of slip amplitude, Wear, 2007, 262 (9), 1159–1170.
- [9] Vingsbo, O. and Soderberg, S. "On fretting maps" Wear, 1988, 126, 131–147.
- [10] Pearson S.R. and Shipway P.H., Is the wear coefficient dependent upon slip amplitude in fretting? Vingsbo and Söderberg revisited, Wear, 2015, 330, 93–102.
- [11] M. Ciavarella, F. Berto, A simplified extension of the Crack Analogue model for fretting fatigue with varying normal load, Theoretical and Applied Fracture Mechanics, 2017,91, 37-43.
- [12] Giannakopoulos A. E., Lindley T. C., and Suresh S., Aspects of equivalence between contact mechanics and fracture mechanics: theoretical connections and a life-prediction methodology for fretting-fatigue. Acta materialia, 1998, 46(9), 2955-2968.
- [13] Majzoobi, G.H. and Jaleh, M., "Duplex surface treatments on AL7075-T6 alloy against fretting fatigue behavior by application of titanium coating plus nitriding," Mater. Sci. Eng. A, 2007, 452–453, 673–681.
- [14] Waterhouse, R.B. and Taylor, D.E. "Fretting Debris and the Delamination Theory of Wear," Wear,1974, 29, 337-344.
- [15] M. Ciavarella, Discussion on "Effect of out-of-phase loading on fretting fatigue response of Al7075-T6 under cyclic normal loading using a new testing apparatus" by F. Abbasi and G.H. Majzoobi, Engineering Fracture Mechanics, 2018, 192, 205-209.
- [16] Yongqing Fu, Jun Wei, Andrew W Batchelor, Some considerations on the mitigation of fretting damage by the application of surface-modification technologies, Journal of Materials Processing Technology, 2000, 99, 231-245.
- [17] Longqiu Li, Izhak Etsion, Frank E. Talke, The effect of frequency on fretting in a micro-spherical contact, Wear, 2011, 270, 857-865.
- [18] B. van Peteghem, S. Fouvry, J. Petit, Effect of variable normal force and frequency on fretting wear response of Ti-6Al-4V contact, Wear, 2011, 271, 1535-1542.
- [19] Hills DA, Nowell D. Mechanics of fretting fatigue. Solid mechanics and its application. Dordrecht: Kluwer Academic Publishers, 1994.



#### **Journal of Mechanical Engineering Research**

http://ojs.bilpublishing.com/index.php/jmer



#### **REVIEW**

#### Remark On Optimal Homotopy Method: Application Towards Nano-Fluid Flow Narrating Differential Equations

#### Farah Jabeen Awan<sup>1</sup> Asif Mehmood<sup>2</sup> and Khalil Ur Rehman<sup>2</sup>\*

- 1. Department of Science and Humanities, National FAST University, Islamabad Pakistan
- 2. Department of Mathematics, Air University E-9 Islamabad 44000 Pakistan

#### ARTICLE INFO

#### Article history:

#### Received: 8 January 2019 Accepted: 8 January 2019 Published: 11 January 2019

#### Keywords:

Non-Spherical nano-Particle Viscous fluid regime

Convergence control parameters

#### ABSTRACT

The short communication is devoted to validate the reliability and convergence of Optimal Homotopy Analysis Method (O-HAM). Owing the importance of present validation of O-HAM one can implement this method towards nanofluid flow narrating differential equations at larger scale for better description. To be more specific, the fractional order differential equation due to vertically moving non-spherical nano particle in a purely viscous liquid and an advection PDE is take into account. The corresponding homotopy for both cases are constructed and solutions are proposed by means of O-HAM. The obtained values are compared with numerical benchmarks. We observed an excellent match which confirms the O-HAM conjecture. Therefore, it can be directed that the utilization of O-HAM towards nanofluid flow regime may provide relief against some non-attempted problems.

#### 1. Introduction

ractional order differential equations have wide range of application in nature. Many scientists and mathematicians are working on fractional calculus [1-2] now a days. It is important to get convergent solution of any physical phenomenon that's why researchers are working to invent or modify the algorithms to solve the problems. An Optimal Homotopy Analysis Method<sup>[3,4,10]</sup> is one of the modified algorithm involving convergence control parameters to speed up the convergence. In current article remark application of Optimal Homotopy Analysis Method (OHAM) towards convergent solutions of fractional order differential equations. To show the efficiency of the method on the physical problems of nature two examples are given representing the fluid flow. For better understating firstly we need to introduce the basics involved in Optimal Homotopy Analysis (OHAM). Consider the following boundary value problem

Khalil Ur Rehman

Department of Mathematics, Air University E-9 Islamabad 44000 Pakistan

Email: khalil.rehman@mail.au.edu.pk

<sup>\*</sup>Corresponding Author:

$$A(u(z,t)) + f(z,t) = 0, z \in \Omega, \qquad (1)$$

$$B\left(u, \frac{\partial u}{\partial t}\right) = 0, \quad z \in \Gamma , \tag{2}$$

where, u(z,t) is a function while z and t denote spatial and temporal independent variables respectively, B is the boundary and A is a differential operator, the domain  $\Omega$  has boundary  $\Gamma$  and f(z,t) is an analytic known function. A can be written as:

$$A = N + L, (3)$$

where,  $L=D_*^a(.)$  is linear (fractional order) and N is nonlinear operator. A Homotopy can be constructed by means of OHAM as follows:

$$\phi(z,t;p):\Omega\times[0,1]\to R,$$
 which satisfies

$$H(\phi(z,t;p),p) = (1-p)\{L(\phi(z,t;p)) + f(z,t)\}\$$

$$-H(p)\{A(\phi(z,t;p)) + f(z,t)\} = 0,$$
(5)

here, p is an embedding parameter where  $p \in [0,1]$  and H(p) represents an auxiliary function which is nonzero. Further, we have following possibilities

H(p) for  $p \neq 0$ .

For 
$$p = 0$$
:  $H(\varphi(z,t;0),0) = L(\varphi(z,t;0)) + f(z,t) = 0$ , (6)  
for  $p = 1$ :  $H(\varphi(z,t;1),1) = H(1)\{(A\varphi(z,t;1)) + f(z,t)\} = 0$ . (7)  
As  $p$  varies from 0 to 1, and the  $\varphi(z,t;p)$  varies from

 $\phi(z,t;0) = u_0(z,t)$  to  $\phi(z,t;1) = u(z,t)$  respectively, where  $u_0(z,t)$  can be obtained from Eq. (5) and Eq. (2). In addition,

$$L(\phi(z,t;0)) + f(z,t) = 0, \qquad B\left(u_0, \frac{\partial u_0}{\partial t}\right) = 0.$$
 (8)

Taylor's series of  $\phi(z,t;p,c_i)$  can be expanded about p as follows:

$$H(p) = pc_1 + p^2c_2 + p^3c_3 + ...$$

$$\phi(z,t;p,c_i) = u_0(z,t) + \sum_{i=1}^{\infty} u_k(z,t;c_i)p^k, \qquad i = 1,2,3,....$$
 (9)

combining Eq. (9) and Eq. (5) and equating the coefficient of like powers of p, we obtain the zeroth-order problem, given by Eq. (8). Similarly, the first and second order problems are obtained as follows:

$$L(u_1(z,t;0)) = C_1 N_0(u_0(z,t)), \quad B\left(u_1, \frac{\partial u_1}{\partial t}\right) = 0, \tag{10}$$

And

$$L(u_{2}(z,t;0)) - L(u_{1}(z,t;0)) = C_{2}N_{0}(u_{0}(z,t))$$
$$+ C_{1}[L(u_{1}(z,t)) + N_{1}(u_{0}(z,t),u_{1}(z,t))], \quad (11)$$

$$B\left(u_2, \frac{\partial u_2}{\partial t}\right) = 0. \tag{12}$$

The general governing equations for  $u_k(z,t)$  are given as follows:

$$\begin{split} L(u_k(z,t)) &= L(u_{k-1}(z,t)) + C_k N_0(u_0(z,t)) + \\ &\sum_{i=1}^{k-1} C_i \big[ L(u_{k-i}(z,t)) + N_{k-i}(u_0(z,t), u_1(z,t), \dots u_{k-i}(z,t)) \big], \\ k &= 2,3, \dots B \bigg( u_k, \frac{\partial u_k}{\partial t} \bigg) = 0, \end{split}$$

(13)

where,  $N_{k-i}(u_0(z,t),u_1(z,t),...u_{k-i}(z,t))$  is the coefficient of  $p^{k-i}$  in the expansion of  $N(\phi(z,t;p))$  about the embedding parameter p and

$$N(\phi(z,t;p,C_i)) = N_0(u_0(z,t)) + \sum_{k>1} N_k(u_0,u_{1,\dots,u_k})p^k.$$
 (14)

The convergence of Eq. (9) depends upon the constants  $C_1$ ,  $C_2$ ,  $C_3$ ..., We take convergent at P=1, therefore

$$\tilde{u}(z,t;C_i) = u_0(z,t) + \sum_{k>1} u_k(z,t;C_i). \tag{15}$$

The residual is obtained by invoking Eq. (15) in Eq. (1), we have

$$R(z,t;C_i) = L(\widetilde{u}(z,t;C_i)) + f(z,t) + N(\widetilde{u}(z,t;C_i)). \tag{16}$$

It is important to note that the  $R(z,t;C_i)$ =0 if solution is n. It is nonzero in case of nonlinear problems. To find the constants  $C_1$ ,  $C_2$ ,  $C_3$ ..., one can use any of the methods available in the literature like Ritz, least squares, Galir-kin's and collocation method to mention just a few. For instance the method of least squares is initiated:

$$J(C_i) = \int_{0}^{t} \int_{\Omega} R^2(z, t; C_i) dz dt, \tag{17}$$

where, R is the residual, so

$$\frac{\partial J}{\partial C_1} = \frac{\partial J}{\partial C_2} = \dots = \frac{\partial J}{\partial C_m} = 0,$$
(18)

the solution of above system of equations will yield an auxiliary parameters. The validation subject to OHAM is elaborated case-wise

#### 2. Non-spherical particle

The vertically falling non spherical particle in purely viscous fluid yield the fractional order differential equation as follows:

$$D_{*_t}{}^{\alpha}u(t) - \frac{w}{q} + \frac{r}{q}u(t) + \frac{s}{q}u^2(t) = 0, \ u(0) = 0, \ 0 \le \alpha \le 1.$$
 (19)

The corresponding homotopy equation can be constructed as

$$(1-p)\left\{\frac{d^{\alpha}u}{dt^{\alpha}} - \frac{w}{q}\right\} - H(p,c_i)\left\{\frac{d^{\alpha}u}{dt^{\alpha}} - \frac{w}{q} + \frac{r}{q}u + \frac{s}{q}u^2\right\} = 0.$$
(20)

Now consider the following relations

$$u(t) = u_0(t) + pu_1(t) + p^2u_2(t)$$
 and  $H(p,c_i) = pc_1 + p^2c_2$ , (21)

By incorporating Eq. (21) into Eq. (20). Further, by regrouping we have following zeroth, first and second order problems

$$\frac{d^{\alpha}u_{0}}{dt^{\alpha}} - \frac{w}{q} = 0, \ u_{0}(0) = 0.$$
 (22)

$$\frac{d^{\alpha}u_{1}}{dt^{\alpha}} - \frac{d^{\alpha}u_{0}}{dt^{\alpha}} + \frac{w}{q} - \left(c_{1}\frac{d^{\alpha}u_{0}}{dt^{\alpha}} - c_{1}\frac{w}{q} + c_{1}\frac{r}{q}u_{0} + c_{1}\frac{s}{q}u_{0}^{2}\right) = 0, \ u_{1}(0) = 0.$$

 $\frac{d^{\alpha}u_{2}}{dt^{\alpha}} - \frac{d^{\alpha}u_{1}}{dt^{\alpha}} - \left(c_{1}\frac{d^{\alpha}u_{1}}{dt^{\alpha}} + c_{1}\frac{r}{q}u_{1} + 2c_{1}\frac{s}{q}u_{0}u_{1} + c_{2}\frac{s}{q}u_{0}u_{1} + c_{2}\frac{d^{\alpha}u_{0}}{dt^{\alpha}} + c_{2}\frac{w}{r} + \frac{r}{r}u_{0} + c_{2}\frac{s}{q}u_{0}^{2}\right) = 0, \quad u_{2}(0) = 0.$ (24)

(23)

By solving Eqs. (22)-(24) we have :

$$u_0 = \frac{t^{\alpha} w}{q \Gamma(\alpha + 1)},\tag{25}$$

$$u_{1} = \left(\frac{t^{\alpha}w}{q\Gamma(\alpha+1)} + \frac{t^{\alpha}w}{q}\left(-(1+c_{1})q + \frac{t^{\alpha}r\sqrt{\pi}4^{-\alpha}c_{1}}{\Gamma(\alpha+\frac{1}{2})}\right)\Gamma(\alpha+1) + \frac{c_{1}st^{2\alpha}w\Gamma(2\alpha+1)}{\Gamma(3\alpha+1)}\right)}{q^{3}\Gamma(\alpha+1)^{2}}.$$
(26)

$$u_{2} = \frac{c_{2}t^{\alpha}w}{q\Gamma(\alpha+1)} + \left(1 + c_{1}\right) \left(\frac{\left(1 + c_{1}\right)t^{\alpha}w}{q\Gamma(\alpha+1)} + \left(1 + c_{1}\right)\left(\frac{\left(1 + c_{1}\right)t^{\alpha}w}{q\Gamma(\alpha+1)} + \frac{t^{\alpha}r\sqrt{\pi}4^{-\alpha}c_{1}}{\Gamma(\alpha+\frac{1}{2})}\right)\Gamma(\alpha+1) + \frac{c_{1}st^{2\alpha}w\Gamma(2\alpha+1)}{\Gamma(3\alpha+1)}\right) + \frac{c_{1}st^{2\alpha}w\Gamma(2\alpha+1)}{q^{3}\Gamma(\alpha+1)^{2}}\right) + \frac{c_{1}st^{2\alpha}w\Gamma(2\alpha+1)}{q^{3}\Gamma(\alpha+1)^{2}}$$

$$\frac{\left(t^{\alpha}w\left(2^{2\alpha+1}{c_1}^2s^2t^{4\alpha}w^2\Gamma(\alpha+\frac{1}{2})\Gamma(2\alpha+1)\Gamma(4\alpha+1)^2+\ldots\right)\right)}{\sqrt{\pi}q^5\Gamma(\alpha+1)^2\Gamma(2\alpha+1)\Gamma(3\alpha+1)\Gamma(4\alpha+1)\Gamma(5\alpha+1)}.$$

By using Eq. (15) the complete solution can be obtained as:

$$u(t) = \frac{t^{\alpha}w}{q\Gamma(\alpha+1)} + \left(\frac{t^{\alpha}w\left(q\left(-\left(1+c_{1}\right)q + \frac{t^{\alpha}r\sqrt{\pi}4^{-\alpha}c_{1}}{\Gamma(\alpha+\frac{1}{2})}\right)\Gamma(\alpha+1) + \frac{c_{1}st^{2\alpha}w\Gamma(2\alpha+1)}{\Gamma(3\alpha+1)}}{\frac{\left(1+c_{1}\right)t^{\alpha}w}{q\Gamma(\alpha+1)} + \frac{\left(\frac{1+c_{1}}{2}\right)t^{\alpha}w}{q\Gamma(\alpha+1)} + \frac{\left(\frac{1+$$

$$+\frac{c_{2}t^{\alpha}w}{q\Gamma(\alpha+1)} + \left(1+c_{1}\right) \left[t^{\alpha}w\left(q\left(-\left(1+c_{1}\right)q + \frac{t^{\alpha}r\sqrt{\pi}4^{-\alpha}c_{1}}{\Gamma(\alpha+\frac{1}{2})}\right)\Gamma(\alpha+1) + \frac{c_{1}st^{2\alpha}w\Gamma(2\alpha+1)}{\Gamma(3\alpha+1)}\right] + \left(\frac{a}{q}\left(s^{2\alpha+1} + \frac{2}{r^{2}} + \frac{2}{r^{2}} + \frac{4a}{r^{2}} $

$$\frac{\left(t^{\alpha}w\left(2^{2\alpha+1}c_{_{1}}^{2}s^{2}t^{4\alpha}w^{2}\Gamma(\alpha+\frac{1}{2})\Gamma(2\alpha+1)\Gamma(4\alpha+1)^{2}+...\right)\right)}{\sqrt{\pi}q^{5}\Gamma(\alpha+1)^{2}\Gamma(2\alpha+1)\Gamma(3\alpha+1)\Gamma(4\alpha+1)\Gamma(5\alpha+1)}+...$$

#### 3. Advection-PDE

The Advection partial differential equation with fractional order is written as:

$$D_{*t}^{\alpha}u(\chi,t)-\chi-\chi t^2+u(\chi,t)\frac{\partial}{\partial \chi}u(\chi,t)=0,\ u(\chi,0)=0,\ 0\leq\alpha\leq1. \tag{29}$$

Using definition of homotopy, we have

$$(1-p)\left\{\frac{\partial^{\alpha}u(\chi,t)}{\partial t^{\alpha}}-\chi-\chi t^{2}\right\}-H(p,c_{i})\left\{\frac{\partial^{\alpha}u(\chi,t)}{\partial t^{\alpha}}-\chi-\chi t^{2}+u(\chi,t)\frac{\partial}{\partial \chi}u(\chi,t)\right\}=0. \tag{30}$$

Now consider the following

$$u(t) = u_0(t) + pu_1(t) + p^2u_2(t)$$
 and  $H(p,c_i) = pc_1 + p^2c_2$ , (31)

by substituting Eq. (31) into Eq. (30) and regrouping one has zeroth, first and second order problem as follows:

$$\frac{\partial^{\alpha} u_0(\chi, t)}{\partial t^{\alpha}} - \chi - \chi t^2 = 0, \ u_0(\chi, 0) = 0. \tag{32}$$

$$\frac{\partial^{\alpha} u_{1}(\chi,t)}{\partial t^{\alpha}} = (1+c_{1}) \frac{\partial^{\alpha} u_{0}(\chi,t)}{\partial t^{\alpha}} - (\chi + \chi t^{2})(1+c_{1}) + c_{1}u_{0}(\chi,t) \frac{\partial}{\partial x} u_{0}(\chi,t), \ u_{1}(\chi,0) = 0, \tag{33}$$

$$\frac{\partial^{\alpha} u_{2}(\chi,t)}{\partial t^{\alpha}} = c_{2} \frac{\partial^{\alpha} u_{0}(\chi,t)}{\partial t^{\alpha}} + (1+c_{1}) \frac{\partial^{\alpha} u_{1}(\chi,t)}{\partial t^{\alpha}} - c_{2}(\chi+\chi t^{2}) + c_{2}u_{0}(\chi,t) \frac{\partial}{\partial \chi} u_{0}(\chi,t) + c_{2}u_{0}(\chi,t) \frac{\partial}{\partial \chi} u_{0}(\chi,t) + c_{2}u_{0}(\chi,t) \frac{\partial}{\partial \chi} u_{1}(\chi,t), \quad u_{2}(\chi,0) = 0.$$
(34)

By solving (32)-(34) one can obtain

$$u_0 = \frac{t^{\alpha} \chi \left(2t^2 + (1+\alpha)(2+\alpha)\right)}{\Gamma(\alpha+3)},\tag{35}$$

$$u_{1} = t^{\alpha} \chi \left( \frac{(1+c_{1})(2+2t^{2}+3\alpha+\alpha^{2})}{\Gamma(\alpha+3)} + \frac{1}{\Gamma(\alpha)} \left( -\frac{1}{\alpha} - \frac{c_{1}}{\alpha} - \frac{2t^{2}}{2\alpha+3\alpha^{2}+\alpha^{3}} - \frac{2c_{1}t^{2}}{2\alpha+3\alpha^{2}+\alpha^{3}} + \frac{4c_{1}t^{2\alpha}\Gamma(2\alpha)}{\Gamma(\alpha+3)\Gamma(1+3\alpha)} + \dots \right) \right),$$
(36)

$$u_{2} = \chi t^{\alpha} \left( \frac{c_{2}}{\Gamma(\alpha+1)} + \frac{2c_{2}t^{2}}{\Gamma(\alpha+3)} + \frac{c_{2}(2+3^{2}\alpha+\alpha^{2}+2t)}{\Gamma(\alpha+3)} + \frac{c_{1}(1+c_{1})(1+\alpha)^{2}(2+\alpha)^{2}t^{2\alpha}\Gamma(1+2\alpha)}{\Gamma(\alpha+3)^{2}\Gamma(1+3\alpha)} + \dots \right),$$
(37)

By using (13) one has the solution as:

$$u = t^{\alpha} \chi \begin{pmatrix} -\frac{c_{2}}{\Gamma(\alpha+1)} - \frac{2c_{2}t^{2}}{\Gamma(\alpha+3)} + \frac{c_{2}(2+3\alpha+\alpha^{2}+2t^{2})}{\Gamma(\alpha+3)} + \frac{(1+c_{1})(2+3\alpha+\alpha^{2}+2t^{2})}{\Gamma(\alpha+3)} \\ + \frac{c_{2}(2+3\alpha+\alpha^{2}+2t^{2})}{\Gamma(\alpha+3)} \end{pmatrix} + \dots,$$
(38)

#### 4. Graphical outcomes

# 

Figure 1. Velocity outcomes for Case-1

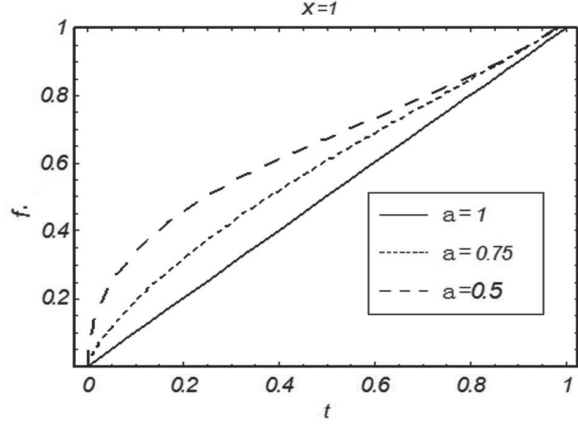


Figure 2. Velocity outcomes for Case-2

#### 5. Table outcomes

**Table 1.** Numerical values and error estimation for

t	Numerical values	Error(Numerical-OHAM)
0.1	0.0956117	0.000749743
0.2	0.18159	0.00247686
0.3	0.257138	0.00444689
0.4	0.321877	0.00587028
0.5	0.375914	0.00610734
0.6	0.419892	0.00486385
0.7	0.45506	0.00236298
0.8	0.483326	-0.00051165
0.9	0.50732	-0.0021004
1.0	0.530455	0.000125035

Table 2. Numerical values and error estimation for and

t	Numerical values	Error (OHAM-VIM)
0.1	0.100027	0.0000273273
0.2	0.200206	0.000205678
0.3	0.300624	0.000623707
0.4	0.401257	0.00125678
0.5	0.501942	0.00194152
0.6	0.602395	0.00239506
0.7	0.702307	0.00230681
0.8	0.801542	0.0015425
0.9	0.900517	0.000517285
1.0	1.00081340	0.00081724733

#### 6. Analysis

In this analysis the reliability and efficiency of Optimal Homotopy Analysis Method (O-HAM) is supported by considering differential system subject to non-spherical nano particle having motion vertically downward and PDE representing advection involvement. The outcomes are offered by way of graphical trends and tabular values. The Figs. 1-2 and Tables 1-2 are provided in this direction. To be more specific, Fig. 1 represents the velocity profiles for different fractional order differential equations have gradual change which ultimately gets closer to velocity profile for  $\alpha=1$ .  $\alpha=0.75$ has convergence control parameters  $c_1 = -0.1229066$ ,  $c_2 = -0.08944891$ ,  $\alpha = 0.5$  has  $c_1 = -0.0364355$ ,  $c_2$ =-0.13012082 and  $\alpha$ =0.25 has  $c_1$ = 0.0128925,  $c_2$ =-0.1637184. From Fig. 2 one can see that towards advection partial differential equation the velocity profiles for different fractional order differential equations have gradual change which ultimately get closer to velocity profile for  $\alpha=1$ .  $\alpha=0.75$ . has convergence control parameters  $c_1$  = -0.1229066,  $c_2$  =-0.08944891 and  $\alpha$ =0.5 has  $c_1$ = -0.723306604,  $c_2$  = 0.2237609808. Table 1 offered the numerical values and error estimation for the velocity of non-spherical particle falling vertically down in the fluid obtained by Optimal Homotopy Analysis Method (O-HAM). The convergence control parameters for Table 1 are  $c_1 = -0.61310285$  and  $c_2 = 0.00034590144$ . Error estimation shows that solution obtained by Optimal Homotopy Analysis Method is in good agreement with exact solution reported in Ref. [11]. Further, the Table 2 represents the numerical values and error estimation for the velocity profile of advection partial differential equation obtained by Optimal Homotopy Analysis Method. The convergence control parameters for Table 2 are  $c_1 = -1.0457108$  and  $c_2 = 0.08153534$ . An error estimation shows that the solution obtained by Optimal Homotopy Analysis Method (O-HAM) is in good agreement with the solution obtained by Variational Iterational Method (VIM) and offered in Ref. [12]. It is trusted that one can implement such method on nanofluid flow narrating differential equation for better solution description.

#### References

- [1] Podlubny I. Fractional differential equations. New York: Academic Press, 1999.
- [2] A. Yildirim and S. T. Mohyud-Din, Analytical approach to space and time fractional Burger's equations, Chinese Physics Letters, 2010, 27 (9), 090501.
- [3] Marinca V, Herisanu N, Nemes L, Optimal homotopy asymptotic method with application to thin film flow. Cent. Eur. J. Phys, 2007, 6(3)648-653.
- [4] Ullah H, Nawaz R, Islam S, Idrees M, Fiza M. The optimal homotopy asymptotic method with application to modified kawahara equation. JAAUBAS. doi: 10.1016/ j.jaubas.
- [5] Herisanu N, MarincaV. Accurate analytical solutions to ossillators with discontinuties and fractional power restoring force by means of optimal homotopy asymptotic method. Comput math Appl. 2010, 60,1607-1615.
- [6] Mohyud-Din ST, Noor MA, Noor KI. Travelling wave solutions of seventh-order generalized KdV equations by variational iteration method using Adomian's polynomials. Int. J. Mod. Phys. B,2009, 23(15), 3265-3277.
- [7] Sajid M, Hayat T. The Application of homotopy analysis method to thin film flows of a third order fluid. Chaos, Solitons and Fractals. 2008, 38, 506-515.
- [8] Mohyud-Din ST, Awan F, Mehmood A. On reliability of homotopy analysis method for equation of vertically falling non-spherical particle. Q Science Connect doi: 10.5339/connect.
- [9] Z. Odibat and S. Momani, Numerical solution of Fokker-Planck equation with space-and time-fractional derivatives, Physics Letters A, 2007, 369, 349-358.
- [10] Anakira NB, Alomari AK, Hashim I. Optimal homotopy homotopy asymptotic method for solving delay differential equations. Math. Prob. Engg, http://dx.doi.org/10.115/2013/498902.
- [11] M. Jalal, D.D. Ganji, G.Ahmadi, Analytical investigation on acceleration motion of a vertically falling spherical particles in incompressible Newtonian media, Advanced Powder Technology, 2010, 21, 298-304.
- [12] J. Ahmad and S. T. Mohyud-Din, An efficient algorithm for some highly nonlinear fractional PDEs in mathematical physics, Plos one, 2014, 9(12). DOI: 10.137/journal. pone.0109127.



#### Journal of Mechanical Engineering Research

http://ojs.bilpublishing.com/index.php/jmer



#### **REVIEW**

#### Macrostructural Analysis of Friction Stir Welding (FSW) Joints

#### Paweł Kossakowski\* Wiktor Wciślik Michał Bakalarz

Kielce University of Technology, Faculty of Civil Engineering and Architecture, Al. Tysiąclecia Państwa Polskiego 7, Kielce, Poland

#### ARTICLE INFO ABSTRACT Friction Stir Welding (FSW) technology is increasingly used in aerospace, automotive, con-Article history: Received: 16 January 2019 struction and other industries. It allows for safe, secure and long-lasting joining of materials Accepted: 18 January 2019 that are difficult to weld or non-weldable with traditional methods. In engineering practice, Published: 25 January 2019 these are primarily aluminium alloys. This article discusses the basic issues related to the FSW technology. The macrostructure of a typical weld is presented. The influence of linear and rotational speed of the tool on the mac-Keywords: Friction Stir Welding (FSW) rostructure of the weld was analyzed (cross-sectional shape, presence of defects). The process Welding parameters of "onion rings" formation in the weld nugget was characterized, taking into account the influ-Aluminium alloys ence of technological parameters on their morphology. Macrostructure "Onion rings"

#### 1. Introduction

In modern technology, there is a significant need for an efficient, reliable and fast method of making high quality welds. This is particularly important in the case of materials whose welding with traditional methods entails significant technological difficulties (eg. aluminium, copper alloys, etc.). The Friction Stir Welding (FSW) technology, despite the relatively high costs, meets these criteria and is increasingly used in industry.

This article presents basic technological issues related to FSW, with particular emphasis on the impact of technological parameters on the weld macrostructure.

#### 2. Friction Stir Welding Technology

Friction Stir Welding with displacement of the weld material was developed and patented in 1991 by W. M. Thomas at the Welding Institute in Cambridge, UK <sup>[1]</sup>. Ultimately, the method was to be used for joining aluminum alloys.

The FSW method is based on the transformation of kinetic energy into thermal energy generated by the friction of the non-consumable tool moving along the edge of contact line. Figure 1 illustrates the FSW process diagram. Friction causes heating and plasticizing of the material in the area of welding. At the beginning of the friction

Paweł Kossakowski

Kielce University of Technology, Faculty of Civil Engineering and Architecture, Al. Tysiaclecia Państwa Polskiego 7, Kielce, Poland Email: kossak@tu.kielce.pl

<sup>\*</sup>Corresponding Author:

stir welding process, heating of the material is caused by the friction between the pin and the plastically deformed material of the joined elements. In the next step, when the resistance rim touches the surface of the material to be joined, most of the energy necessary to heat the material is obtained from the friction between the shoulder and the surface of the material being joined [2]. During penetration, a cylindrical tool ended with a shoulder and a profiled pin rotates, introducing the plasticized material into a whirl movement [3]. In this way, it is displaced in the direction of rotation of the tool, which can be either clockwise or counter-clockwise. As a result, we obtain an asymmetrical connector, which consists of the advancing side and the retreating side. The advancing side occurs in the place where the material flows in the direction of the moving tool, in the opposite situation we are talking about the retreating side. These sides differ from each other in terms of the size of their own stresses, strains and microstructure [4].

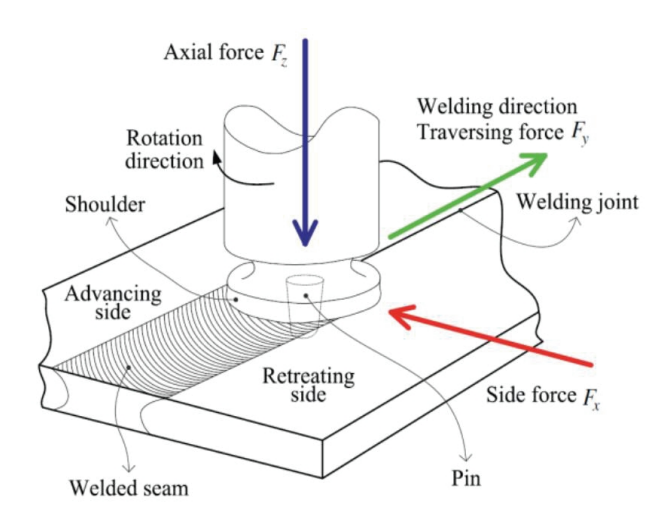


**Figure 1.** Scheme of the FSW process <sup>[5]</sup>

The basic parameters of the friction welding process are: the shape of the mixing tool, the welding speed, the rotational speed of the tool, the angle of inclination of the tool to the welded surface and the pressure force [3]. Among the above parameters, the shape of the tool is considered one of the most important factors in the process of friction stir welding. It affects the flow of material, and thus the quality of the weld obtained and the type of defects that may arise after the welding process. The FSW tool consists of a shoulder and a pin, and its detailed design may differ due to the shape, diameter and length of the pin and shape, the diameter of the shoulder surface [6]. Figure 2 illustrates the FSW tool diagram. Due to the intensive development of FSW technologies in the last two decades, the impact of welding process parameters on the quality of the weld obtained was discussed in numerous publications [7-10].

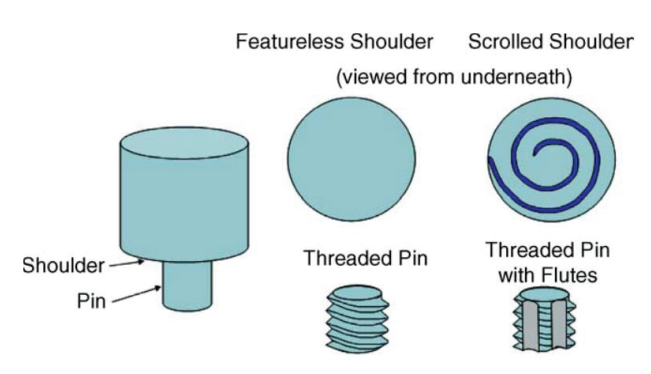


Figure 2. Scheme of FSW tool<sup>[6]</sup>

Most often, the following factors are given as the advantages of friction stir welding with mixing of the weld material [3,6]:

- a. high static and dynamic strength properties of the joints:
- b. favorable metallurgical properties: slight distortion of the working area, good microstructure, no cracks;
- c. dimensional stability and repeatability due to process automation;
- d. the method is ecological and safe, because it does not cause emission of welding gases and dusts, formation of magnetic fields and noise; does not require the use of solvents for surface degreasing and shielding gases;
- e. low consumption of materials and short process preparation time due to the lack of cleaning, grinding, brushing or surface pickling;
- f. the aesthetic look of the weld surface, often requiring no further processing;
- g. reduction of energy consumption due to the possibility of better use of combined materials.

However, the disadvantages of FSW methods are [2]:

- h. dimensions of the welding device make it a stationary method;
- i. the need to use higher quality tool material, adapted to the material properties of the combined metals;
- g. the necessity of using rigid holders for fixing welded elements that prevent moving of the joined panels during the process;
  - k. limitation of the tool life and its high cost.

#### 3. Macrostructural Analysis of Few Joint

#### 3.1 Weld Structure [6]

Similarly to conventional weld, in the FSW joint a few characteristic areas in the cross-section can be distinguished (Fig. 3):

- joint nugget,
- thermo-mechanically affected zone (TMAZ),
- heat-affected zone (HAZ).

The specific process of welding takes place in the nugget (or dynamically recrystallized zone - DXZ). Due to the plastic deformation and frictional heat the nugget zone undergoes recrystallization, i. e. formation of fine grains. The grain size changes in the weld cross-section. The biggest grains were observed in the upper area of the weld, whereas smaller grains were observed at the bottom [11]. The grain size distribution described above is believed to be the effect of temperature gradient during welding, i.e. higher temperature produced at the upper side of the weld by the tool results in the formation of larger grains. The welding tool motion produces the structure of the so called "onion ring" in this area (see Fig. 3). As indicated in many papers, for example [12-14], the motion of FSW tool causes the dissolution of the inclusions. As a result, fewer inclusions occur in the area of the weld nugget and they are smaller than in the parent material.



Figure 3. Typical FSW joint structure, according to [6]

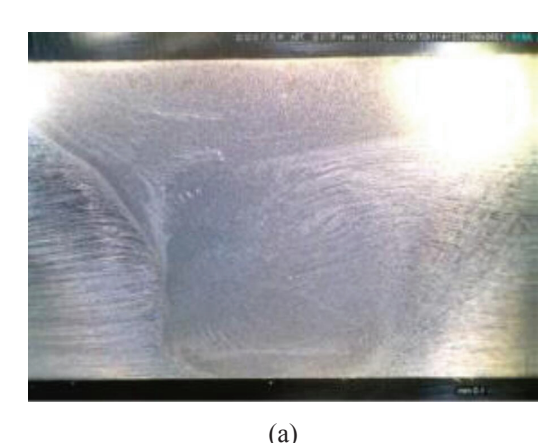
Thermo-mechanically affected zone (TMAZ) plays the role of transition area between the nugget and heat-affected zone. Although this area is characterized by considerable deformation, the strain values are too low to cause grain recrystallization. On the other hand, a significant increase in temperature causes the dissolution of some precipitates, and thus the change in the microstructure of the material [15].

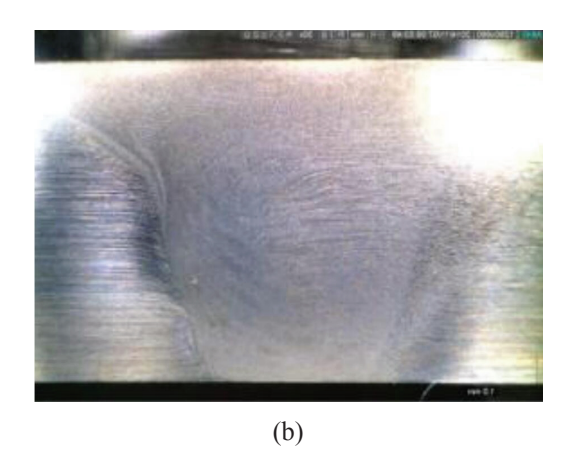
The heat affected zone (HAZ) is not subjected to significant plastic deformation, therefore the microstructure of the grains is similar to the native material. However, the elevated temperature results in a reduction in the amount and change in the structure of inclusions and precipitates.

### **3.2** Effect of Tool Travel and Rotation Speed on the Weld Macrostructure [16]

An interesting insight into the effect of FSW process parameters (rotation and travel speed) on the joint shape is presented in <sup>[16]</sup>. The authors analyzed friction stir welding of Al2195-T8 Al-Li alloy. During the experiment, plates with a thickness of 7.4 mm were welded together with the use of cone shape threaded pin and threaded surface of shoulder. Displacement controlled shoulder - to plate pressure was applied in order to provide shoulder contact with the material being processed.

Effect of travel speed on the FSW joint shape is demonstrated in Fig. 4 a-c. The welds illustrated in Fig. 4 were prepared at the fixed tool rotation speed 600 rpm. In each picture the left side of the photograph represents the advancing side, i.e. area, where tangential direction of rotation is consistent with the travel direction.





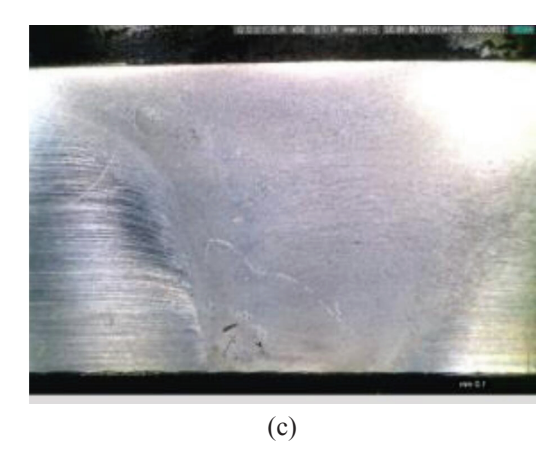


**Figure 4.** Effect of travel speed on the weld macrostructure: a) 120 mm/min, b) 300 mm/min, c) 420 mm/min (rotation speed 600rpm) [16]

As shown in Fig. 4, the weld boundary is sharper on the advancing side, while on the retreating side the border is indistinct. The results obtained by the authors of [16]

clearly confirm the effect of the tool linear speed on the shape of the weld cross-section. For the lowest speed of 120 mm/min (Fig. 4a), the shape of the bottom part of the joint is regular, close to the square. Increasing the speed of the tool causes irregular shape of the welds. At the top speed of 420 mm/min (Fig. 4c), on the advancing side macrodefects were observed. As the authors point out, the use of excessive speed of the tool may result in a tunnel effect, i.e. the formation of a linear defect along the weld. The authors of [16] performed the similar analysis for different tool rotational speeds (Fig. 5 a-c) and constant travel speed 240 mm/min. As before, the increase in the speed of the tool caused an irregular weld shape on the advancing side. The highest quality of the weld was obtained for the speed of 300 rpm. Increasing the tool rotation speed resulted in irregular shape of the weld, especially on the advancing side.

# 3.3 Effect of the Process Parameters on "Onion Rings" Formation in the Weld Nugget [17]

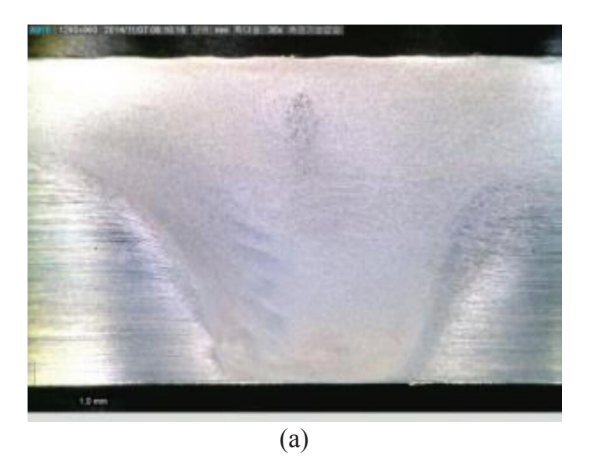
As mentioned, the characteristic feature of friction stir welding technology is the formation of the so-called "onion rings" in the weld nugget. Depending on the technological parameters of the process, the rings may have different structure.

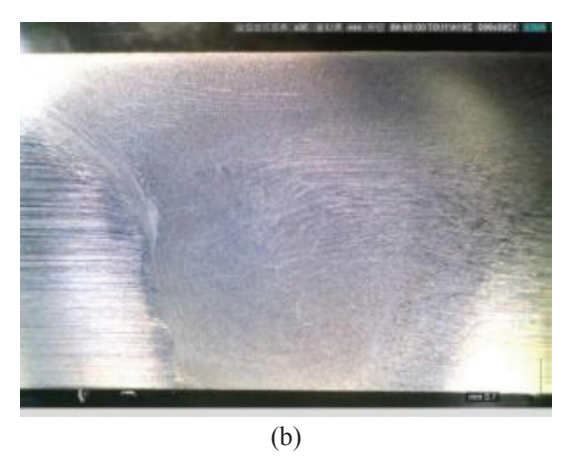
The author of the paper <sup>[17]</sup> discussed the effect of rotational and travel speed of FSW tool on the macrostructure of the weld nugget.

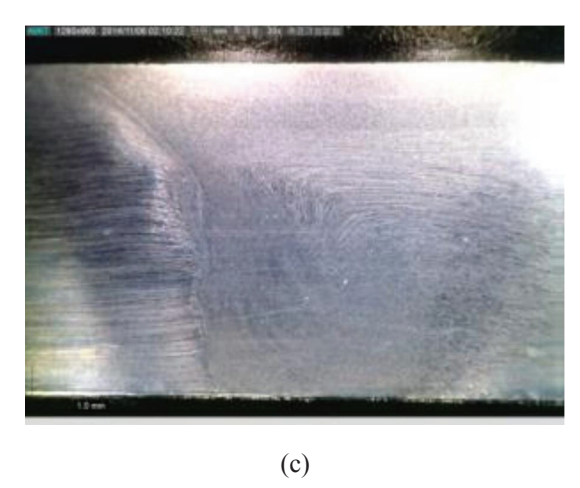
In order to analyze the FSW macrostructure, elements made of aluminium alloys 6061 and 7075 were welded together. Welds were prepared at the tool speeds of 400, 800 and 1440 rpm, while the welding speeds were 120 and 288 mm/min. The author has not provided information concerning the shape of FSW tool and the geometry of welded elements. In the next stage transversal and longitudinal sections of welds were prepared and then subjected to macrostructural observations.

Figure 6 presents an example of the structure of "onion rings" in the weld nugget. In the cross-section of the weld (Fig. 6a), characteristic ring structures are visible. The rings spacing is larger in the middle part of the weld, but decreases as it approaches its edges.

Figure 6b shows the longitudinal section of the weld. The rings from Figure 6a are in this case visible in the form of characteristic band structures. In the lower and middle parts of the weld, the bands are deflected in the direction opposite to the travel direction of the tool. In the upper part of the weld, the bands have a direction similar to vertical, which, according to the author of the work [17], results from the effect of the shoulder on the location of the mixed material. Figure 6c shows a three-dimensional



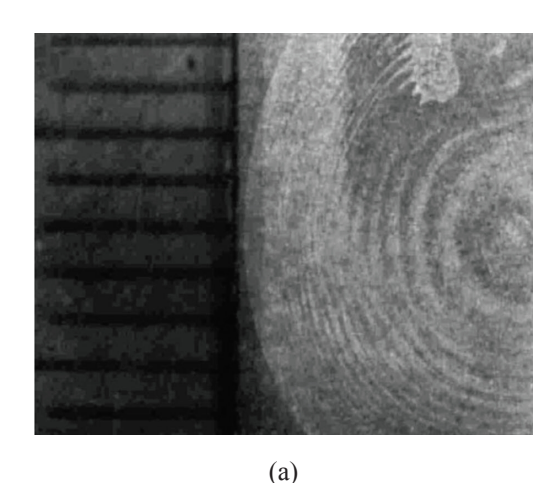


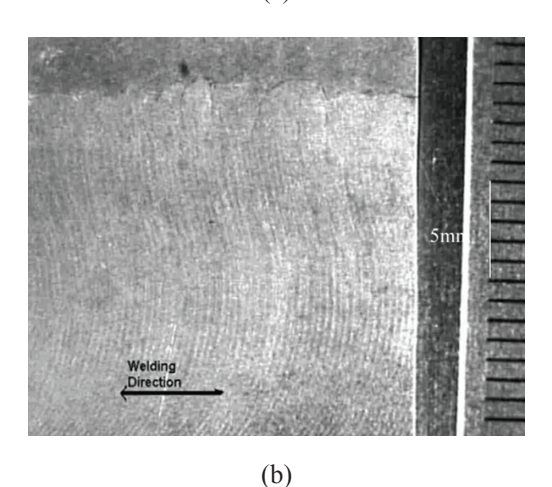


**Figure 5.** FSW weld macrostructures for different tool rotation speeds: a) 300 rpm, b) 600 rpm, c) 800 rpm, travel speed 240 mm/min [16]

visualization of the distribution of circles/bands in the weld nugget structure.

In Figure 6c, the characteristic semicircular structures on the upper surface of the weld are visible. Their presence results from the direction of material movement around the tool. The process starts with the material layer heating up due to the friction resulting from the rotary





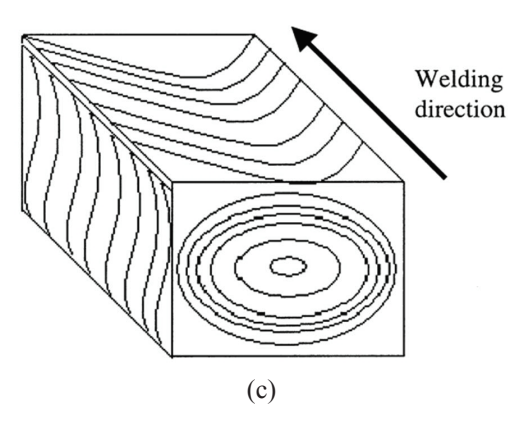


**Figure 6.** Structure of "onion rings" in Al alloy weld nugget: a) weld cross section, b) weld longitudinal section, c) 3D view of weld nugget with "onion rings" pattern [17]

movement of the tool. Then, the hot and plasticized material is passed over the tool, forming a weld and creating semi-cylindrical bands. As shown in [17], the distance between bands is equal to the tool travel distance during its single rotation. In addition, the weld morphology (band structure) results from the fact that the material heating by friction is not an immediate process. It requires a certain

period of time, which results in periodic arrangement of the bands in the weld.

Figure 7, derived from <sup>[17]</sup>, illustrates the effect of linear and rotational velocity of the tool on the band spacing. As can be seen, the increase in rotational speed results in reduction in the band spacing, with the largest differences being observed in the rotational speed range below 1000 rpm. As expected, the increase in the linear speed of welding caused an increase in the spacing of bands in the weld. It should also be noted that, according to Figure 7, the use of different combinations of linear and rotational speed of the tool leads to the same spacing of bands in the joints.

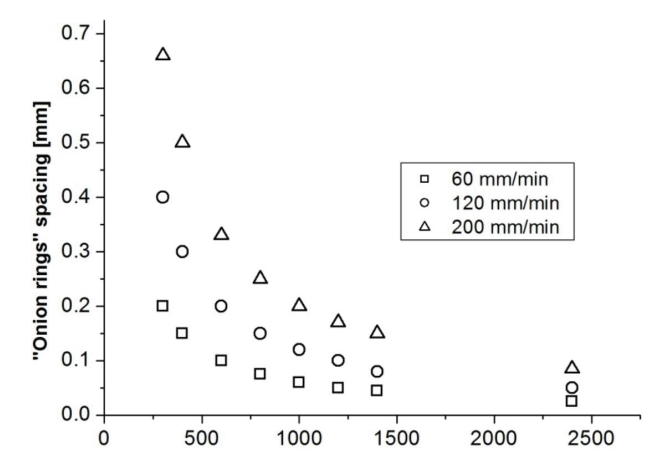


**Figure 7.** Effect of the FSW process parameters (tool travel and rotation speed) on "onion rings" spacing in the weld [17]

## 3.4 Joint Defects as a Result of Process Parameters $^{[16]}$

It is to be expected that the method of forming a weld in the FSW process (extruding the heated material) can cause defects (voids) behind the tool, and thus in the prepared joint.

In the previously mentioned work <sup>[16]</sup> an analysis of the influence of linear and rotational speed of the tool on the formation of weld defects (voids, discontinuities) was made. Welds, made in the manner described before, were used for this purpose. Finished welds were X-rayed. The results of the observations are presented in Figure 8.

The increase in the linear velocity, although it allows for a significant reduction in the weld time, in the whole analyzed range of rotational speeds resulted in the appearance of joint defects.

As it results from the graph analysis, the change in rotational speed in the range from 300 to 800 rpm did not cause the deterioration of the weld quality.

As shown in [18], further increase in the rotational speed of the tool (over 1000rpm) was the cause of significant weld defects, affecting element strength.

#### **About the Publisher**

Bilingual Publishing Co(BPC) is an international publisher of online, open access and scholarly peer-reviewed journals covering a wide range of academic disciplines including science, technology, medicine, engineering, education and social science. Reflecting the latest research from a broad sweep of subjects, our content is accessible worldwide – both in print and online.

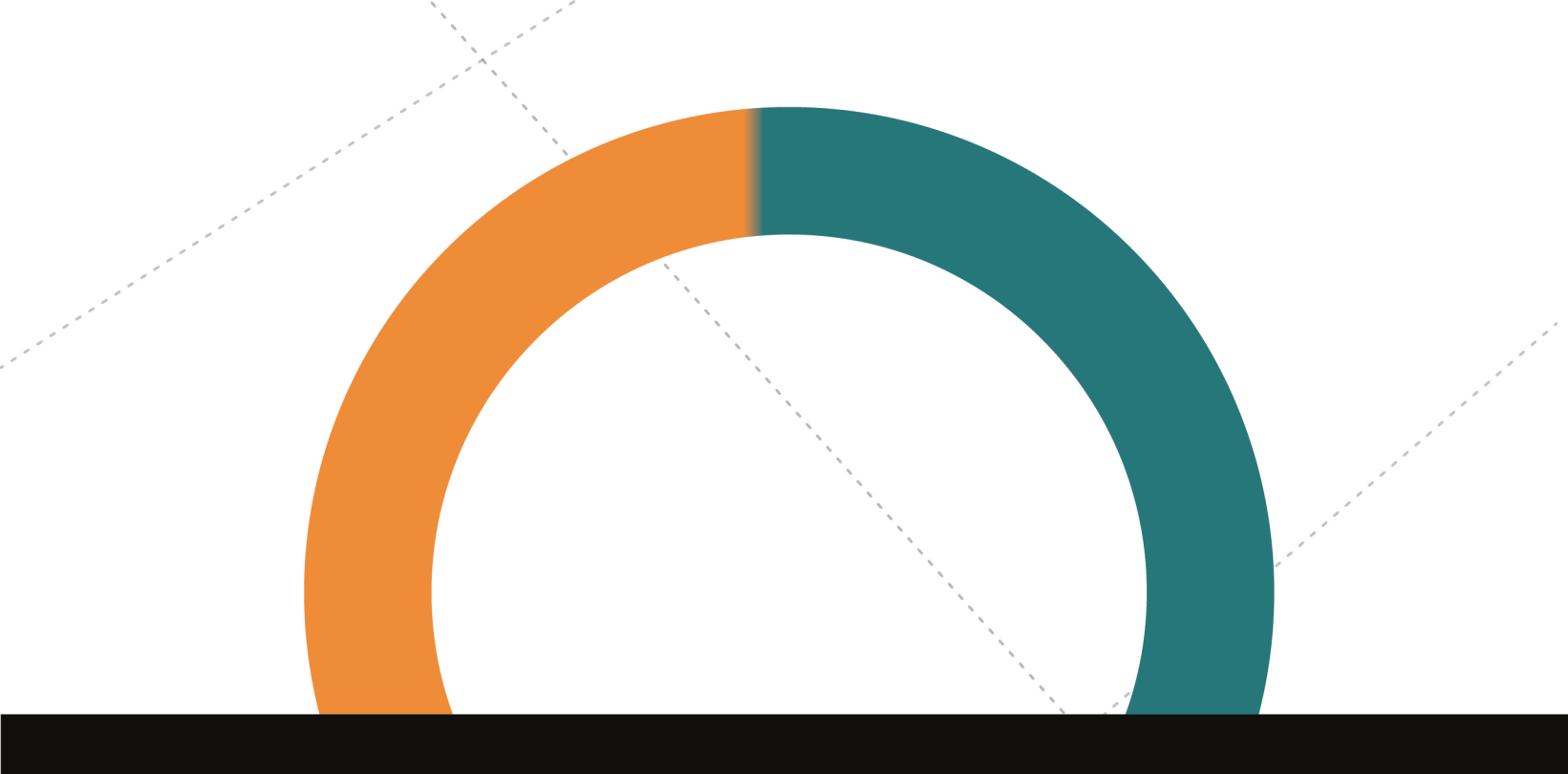
BPC aims to provide an academic platform for academic exchange and cultural communication that help organizations and professionals in advancing society for the betterment of mankind. BPC hopes to be indexed by well-known databases in order to expand its scope to the science community, and eventually grow to be a reputable publisher recognized by scholars and researchers around the world.

BPC adopts the Open Journal Systems, see on ojs.bilpublishing.com

#### **About the Open Journal Systems**

Open Journal Systems (OJS) is sponsored by the Public Knowledge Project Organization from Columbia University in Canada, jointly developed by PKP, the Canadian Academic Publishing Center and Canada Simon Fraser University Library. OJS can realize the office automation of periodical editing process, station build and full-text journals by network publishing. The system design is in line with international standards, and supports peer review. It is very helpful to improve the citation rate, academic level and publication quality of periodicals.





Bilingual Publishing Co. is a company registered in Singapore in 1984, whose office is at 12 Eu Tong Sen Street, #08-169, Singapore 059819, enjoying a high reputation in Southeast Asian countries, even around the world.



Tel:+65 65881289
E-mail:contact@blipublishing.Com
Website:www.Blipublishing.Com

